SIMULATION AND OPTIMIZATION OF THERMO-FLUID SYSTEMS: MICROCHANNEL COOLING AND OTHER APPLICATIONS

by

XIAOBING ZHANG

A dissertation submitted to the

School of Graduate Studies

Rutgers, The State University of New Jersey

In partial fulfillment of the requirements

For the degree of

Doctor of Philosophy

Graduate Program in Mechanical and Aerospace Engineering

Written under the direction of

Yogesh Jaluria

and approved by

_____

_____

_____

_____

New Brunswick, New Jersey

January 2020

ABSTRACT OF THE DISSERTATION

Simulation and optimization of thermo-fluid systems: Micro-channel cooling and other applications

By XIAOBING ZHANG

Dissertation Director:

Yogesh Jaluria

Microchannel systems for cooling applications such as in thermal management of electronic equipment are investigated and optimized under deterministic and reliability conditions. Numerical simulations are carried out to study the conjugate heat transfer and flow behavior. The numerical model has been validated by comparing with analytical and experimental results. Uncertainties are often significant in the operating and design of thermal systems. Any minor variations in the design variables or operating conditions may lead to system failure. In this study, a microchannel cooling system for a 1 cm x 1 cm electronic chip is studied and optimized under design uncertainties. Three significant design variables or operating conditions are considered: (1) flow rate, (2) channel width or the number of channels, (3) heat flux. The standard deviations for the design variables, which are assumed to be normal distributions, are taken as 5% of the mean values. The acceptable probability of failure is chosen as 0.13%, which is the usually accepted level in

reliability studies. Response surfaces are used to represent the thermal and fluid behavior in the microchannel systems. Based on the Polynomial Response Surface (PRS) modeling results, a multi-objective optimization problem is formulated to reduce both pumping power and thermal resistance. Two major practical concerns, hot-spot temperature and pressure difference serve as constraints. With varying weights on the two conflicting objectives, Pareto frontiers for deterministic and reliability cases are determined and compared. The differences demonstrate the importance of uncertainty in the microchannel cooling applications. This study provides more reliable and realistic design solutions for microchannel cooling systems.

This approach may be extended to the simulation, design and optimization of other thermal problems and processes. In this study, the selective laser melting (SLM) gas chamber and chemical vapor deposition (CVD) systems are simulated and optimized as well. It is proven that this basic approach presented here is applicable to a wide variety of thermal fluid systems. Similar concerns and trends arise in the modelling and design of these systems.

Acknowledgements

Dr. Yogesh Jaluria is my academic tutor and life mentor. Dr. Jaluria was my co-advisor when I was doing my master's degree at Rutgers. I was in an extremely terrible situation in the very last days of my master. During that period, he provided me hope and support in the worst days of my life. I can hardly imagine what might happen without Dr. Jaluria. In my academic research, Dr. Jaluria's deep understanding of thermal physics helped resolve one by one difficult problems.

Besides, I want to thank Dr. Zhixiong Guo and Dr. Javier Diez for being my committee members and provide me guidance in classes. I also owe a thanks to Dr. Charles Tuffile and Dr. Bo Cheng for providing me extremely valuable opportunities at Bosch Research.

On my family side, I want to thank the most is the love of my life, my wife Qiaoqiao Zhu. She can always warm my heart when life is not as expected. I believe our life will be more colorful in the future. I also want to thank my mother, Cuizhi Zhang, my father, Wenbiao Zhang, and my sister, Xiaoyan Zhang for their understanding and support. Another family member is my precious white miniature schnauzer. His name is Beta Bonita Zhang Zhu. Life is full of fun ever since we had him.

In the last, I want to thank my friends, my lab mates, my classmates, MAE staff and others who had helped me.

Contents

List of illustrations

Nomenclature

A_s	Plate surface area, m^2
$\vec{g}$	Gravitational acceleration, m/s^2
c_p	Specific heat at constant pressure, $J/(kg \cdot K)$
k	Thermal Conductivity, $W/(m \cdot K)$
K_n	Knudsen number
L	Length, m
L_c	Characteristic length, m
$\dot{m}$	Mass flow rate, kg/s
N	Number of channels $N \cong 10^4/(2W)$
p	Pressure, Pa
Nu	Nusselt number
$p_{x,y}$	Polynomial coefficients
$Power$	Pumping power, W
$Pressure$	Pressure drop, Pa
q''	Heat flux, W/cm^2
$HotT$	Hot-Spot Temperature, K
Ra	Rayleigh number
T	Temperature, K
d	Optimal solution
G_U	System performance function in u-space
g	Constraint function
h	Heat transfer coefficient
P	Probability
R	Thermal resistance
u	The standard normal design variable
$\vec{v}$	Velocity

W	Channel width
X	Non-normal system parameter

Greek symbols

$\dot{v}$	Velocity, m/s
$\dot{V}$	Volume flow rate, ml/min
δ	Lattice spacing, m
λ	Mean free path, m
θ	Thermal resistance, $℃ \cdot m^2/W$
μ	Dynamic viscosity, $kg/(m \cdot s)$
ρ	Density, kg/m^3
ω	Weight factor
σ	Standard derivation
β_G	Reliability target index
Φ	Standard normal cumulative distribution function

Subscripts

sub, avg	Substrate averaged
in	Channel inlet
max	Maximum
$*$	Target probability performance measure

Subscript

f	Failure
∞	Far from a surface

1 INTRODUCTION

In this study, the optimization of several thermal systems, particularly microchannel cooling systems, is carried out. Both deterministic and reliability optimization approaches are investigated. In this chapter, the motivation, objectives, and literature review of the work are given. In Chapter 3 and Chapter 4, the deterministic and reliability optimization methods are presented. These methods are used directly for the microchannel cooling system. In Chapter 5, we broaden the optimization to the Selective Laser Melting (SLM) and Chemical Vapor Deposition (CVD) applications.

1.1 MOTIVATION & OBJECTIVE

As an important branch of microelectromechanical systems (MEMS), microchannels have many advantages as compared to traditional macro-size channels [1]. With microchannels, many impractical missions become achievable, such as small volume liquid transport, high heat flux cooling and low energy consumption. In biological applications, microfluidics devices can be used in drug delivery, cell/protein separation and many other lab-on-chip tasks [2]. Many industrial applications require cooling of components with very high heat flux inputs. One typical application is the cooling of electronic microchips. As the number of transistors in one microchip approximately doubled every decade, the heat load increased at the same time. The heat flux inputs are typically so high that traditional macro-size cooling method can no longer handle the heat removal.

Many researchers have successfully developed systems to increase the heat flux limitation with the help of microchannels [2-4]. Lee et al. [5] experimentally tested the microchannel cooling possibility of removing heat flux inputs up to 45 W/cm^2.

Kandlikar and Grande [3] proposed a single-phase microchannel design that can handle heat flux values up to 100 W/cm^2. Sui et al. [6] designed a wavy-structure microchannel that is able to remove up to 300 W/cm^2using computational studies. Using multi-phase liquid cooling, flow boiling or modified geometry configurations [7-11], these heat flux limits can be further increased.

In the internal pipe flow applications, microchannels can achieve very high heat transfer coefficients as its hydraulic diameter sizes down. This makes microchannel systems excellent heat removers for electronic cooling and other applications. However, it has drawbacks. One disadvantage is the high pressure drop which may shoot up to several atmospheres. Such a high pressure-drop might cause leakage, and destroy sealing, substrate, pumps or even the entire system. In such cases, it is required to either switch to larger size channels or reduce the liquid flow rate. Both cases increase the device hot-spot temperature, thus lowering the system cooling performance. Therefore, there are two objectives in the design of a microchannel heat removal system. The first is to reduce the overall thermal resistance. The second is to keep the pressure difference within an acceptable range. This leads to an optimization problem.

In this work, microchannel systems to remove energy from a relatively small area are studied. Extensive numerical simulations are carried out. Parametric modelling in terms of two sets of design variables is implemented. Based on the Polynomial Response Surface (PRS) results, single-objective, multi-objective and Pareto optimizations are performed. Also, this paper investigates some practical concerns such as the pressure drop and hot-spot temperature limitations. These two limitations will serve as constraints in the optimization formulation. An optimal configuration is also predicted. In this study,

reliability optimization of the microchannel cooling system for a 1cm by 1cm electronic chip is performed. Two major design constraints are taken as the pressure drop constraint and the hot-spot temperature constraint. A normal distribution with a 5% or 10% standard derivation is used for the flow rate and heat flux input. Two separate sets of design variables are examined.

1.2 LITERATURE REVIEW

Three thermal and fluid systems are studied in this study: the microchannel cooling system, the SLM gas flow system for additive manufacturing, and the CVD system. The associated research work and the optimization are reviewed in detail.

1.2.1 Literature review on optimization of microchannel cooling systems

The research on optimization of microchannel cooling is quite limited [4, 7]. The available research has not considered the constraints from the pressure drop and hot-spot temperature in detail [12]. Under pressure and temperature constraints, channels with smaller hydraulic diameter do not always yield a better performance. In fact, there exists a maximum feasible heat flux for a given geometry [3]. The pressure drop penalty and other design constraints are often neglected. High heat flux is desirable, but pressure drops of a few bars or pumping powers of several watts are not practical [13, 14]. The failure possibility from a constraint like hot-spot temperature should also be taken into considerations. In microchannel designs, we want to achieve high thermal performance. On the other hand, the pumping power is to be controlled within a reasonable range. A good microchannel design must satisfy these two conflicting objectives simultaneously.

Optimization is necessary for designing robust and reliable microchannel cooling devices. Husain et al. [12] studied the microchannel geometry effects and obtained the

Pareto frontiers for optimization. The design and optimization work for straight and other shapes microchannels is also carried out [15, 16]. Zhang and Jaluria [17] studied the deterministic optimization formulation of microchannel cooling applications under different design constraints.

In practical applications, uncertainties in the design variables or the operating conditions are unavoidable. Moreover, an optimal design guided by deterministic optimization might not be reliable enough to survive the range of working conditions. An optimization formulation that handles design uncertainty is usually named reliability optimization or probabilistic optimization [18]. Tu et al. [19, 20] introduced the performance measure approach (PMA) that is shown to be more robust compared to the more common reliability index approach (RIA). George et al. [21] applied this PMA in the reliability optimization of chemical vapor deposition systems. In terms of microchannel applications, reliability optimization research is minimal. Sarangi et al. [22] completed the optimization under uncertainty for manifold microchannel systems with a uniform design variable distribution. Reliability optimization for regular straight microchannels with a relatively more realistic Gaussian distribution is rare. Uncertainties in the fabrication processes is another factor that is seldomly considered [23, 24].

1.2.2 Literature review on selective laser melting gas flow system

In selective laser melting (SLM) process, a high-energy laser beam is utilized to melt and fuse the metallic powder materials. The resulting high local temperature can easily exceed the material evaporation point and cause evaporation. The complicated vaporization effect may cause a “vapor-jet” effect, leading to the generation of emissions. The emissions include the vaporization gases, “vapor jet” entrained powders, and liquid droplets ejected

from melt pool due to melt pool dynamics. Therefore, the spatter (ejected particles from or around melt pool) mainly consists of droplet spatter and powder spatter [25]. Numerical modelling has been utilized to understand the complex physics in powder bed additive manufacturing process. Lee and Zhang [26] developed a discrete element method (DEM) model to simulate the powder spreading process in SLM. In addition, a computational fluid dynamics (CFD) model is developed to investigate the melt pool dynamics with the incorporation of DEM generated powder bed. The thermal information was utilized to calculate solidification morphology and grain size. Panwisawas et al [27] simulated the positions of powder particles in a powder bed by dropping spheres based on encountered obstacles. Micro-scale CFD simulations were performed to establish the relationship between laser process parameters, melt pool and microstructure. Shrestha and Chou [28] modeled the two-layer powder deposition process in SLM.Their simulation showed interlayer lack-of-fusion phenomenon if a high laser scanning speed was applied. Using both DEM and CFD modelling tool, Cheng et al [29] studied the powder spreading condition on melt pool characteristics in SLM process. A higher powder bed packing density, caused by smaller roller rotational speed, lead to smaller re-melting depth. Lawrence Livermore National Laboratory (LLNL) utilized the arbitrary Lagrangian-Eulerian (ALE) package to study various physical processes such as melt pool dynamics, scanning track surface morphology, and melt pool emission [30-33]. A comprehensive review of additive manufacturing process thermal analysis and simulation can be found in literature [34]. However, it is very difficult to simulate the spatter motion over the entire build chamber using the micro-scale melt pool model.

On the other hand, spatter characteristics can be studied by experimental measurement. Using the high-speed X-ray imaging technology, Zhao et al [35] were able to obtained important spatter parameters such as spatter count, diameter, and velocity with respect to different scanning speeds and laser powers. Their observations indicated that larger speed spatters could be generated from higher laser power conditions. Gunenthiram et al [36] also experimentally analyzed the formation of spatters in SLM process. By introducing a high-speed imager in SLM system, they quantified the spatter ejections as well as possible correlation with melt pool dynamics. Their results showed that larger sized spatters could be generated for SS316L material if high laser volume energy density was applied on powder bed. On the other hand, the droplet might be incorporated into melt pool area for Al-12Si material, thus higher spattering was observed on SS316L powder bed.

Without any removal process, the spatters may re-deposit on the powder bed due to gravity and contaminate the build area, potentially affecting the build part quality. In common practice, a shielding gas flow can help to remove the ejected particles. However, the spatter removal efficiency heavily depends on the design and optimization of the gas flow system in the build chamber. Studies about the gas flow system are sparsely found in the literature. Philo et al [37, 38] developed a CFD model to study the gas flow characteristics inside the Renishaw AM250 build chamber. The movement of spatters was simulated by discrete phase method (DPM). The simulated velocity field in the chamber was validated against the flow field obtained by Hot Wire Anemometer (HWA) measurement. They found that the flow uniformity and average flow velocity could be influenced by inlet rail radius and inlet/outlet height. Wang and Chang [39] tried to optimize the flow uniformity inside a selective laser sintering (SLS) system. A CFD model

was utilized to investigate the effect of influential factors on flow velocity profile and uniformity, e.g., the trapezoid push nozzle, the suction tunnel and nozzle-to-plane distance. However, optimal design and modelling for build chamber to increase spatter removal rate, especially considering gas flow – spatter interaction, is still not thoroughly investigated.

The optimization work regarding SLM gas flow system is extremely rare. In this study, parameters like volume flow rate, channel inlet and outlet locations, and other various aspects are examined. Some preliminary optimization work is performed.

1.2.3 Literature review on chemical vapor deposition system

Chemical vapor deposition system (CVD) is commonly used in the fabrication of solar cells, optical fiber, semiconductor devices, and other applications where thin-coatings are necessary [40]. In recent years, CVD method is also applied in the graphene and carbon nanotubes manufacturing [41]. The CVD process produces high-purity, low-cost, and large-scale thin-films.

Gallium Nitride (GaN) is an advantageous material in the light emitting diodes (LED), transistors, and other semiconductor applications. One way to fabricate GaN is the hydride vapor phase epitaxy (HVPE) process. This method is low efficiency, and the fabricated films are heavily contaminated. Metal Organic Chemical Vapor Deposition (MOCVD) was first invented by Kawabata et al. [42]. Later, this process was improved by many researchers. Even so, there are many MOCVD process problems in the mass production phase. The improvement of growth rate and film uniformity is one of the major industry problems. In this study, the optimization of CVD system will be done with respect to TMG flow rate and system pressure. The radial basis function is used for parametric studies.

1.3 RESEARCH CONTRIBUTIONS

The featured research contributions are listed below:

(1) The conjugate heat transfer model is developed and validated. The response surfaces to model the numerical results are made regarding different sets of design variables.

(2) The pressure-drop and hot-spot temperature are taken into consideration and serve as the design constraints.

(3) A validated deterministic model is built to calculate the Pareto frontiers of the microchannel cooling systems. The Pareto solutions could provide important practical guidance to industrial applications.

(4) A converged and robust reliability model is developed based on the Performance Measure Approach (PMA)

(5) The reliability optimization with Gaussian distributed design variables are achieved.

(6) The numerical simulation for SLM gas flow system is completed. And simple optimization work regarding this system is implemented.

(7) The radial basis function (RBF) is used in the response surface models of the CVD system. This RBF method could capture the local behavior more accurately.

2 MATHEMATICAL MODELLING OF MICROCHANNEL-BASED COOLING SYSTEM

To study the performance and behaviour of a small area microchannel system, a conjugate heat transfer model for a single microchannel section was developed and simulated. The entire system is formulated by repetition of these single channel sections with periodic boundary conditions. GAMBIT is used to build the mesh [43], and the finite volume method, based on ANSYS FLUENT [44], was employed to solve the energy, momentum and continuity governing equations. The heat conduction equation is used to calculate the solid substrate temperatures. Grid independence was tested together with validation by comparisons with analytical results for fully developed flow.

2.1 GOVERNING EQUATIONS AND SYSTEM DESIGN

In this study, the microchannel hydraulic diameter ranges from 20 to 100 μm. Water is used as the cooling fluid. There is no mean free path for liquid, but the lattice spacing δ can be used to replace mean free path. For water, the lattice spacing is approximately 0.3 nm [45]. Within this diameter range, the Knudsen number, defined in equation below, is smaller than 0.001 and the continuum model can be applied [46].

$$Kn = \bar{\lambda}/L \tag{1}$$

The fluid inside this microchannel system behaves as a single-phase, no-slip, laminar flow. Polydimethylsiloxane (PDMS) is used as insulation material on top of the system. Silicon is used as the substrate material, because it is widely used in the semiconductor industry and the fabrication techniques are well established [47, 48]. This study only considers rectangular microchannels and the effect of the shape and profile is not studied.

The equations for the conservation of mass, momentum and energy that are solved to get the steady-state solutions are:

$$\nabla \cdot \vec{v} = 0 \tag{2}$$

$$\nabla \cdot (\rho \vec{v} \vec{v}) = -\nabla p + \rho \vec{g} + \nabla \cdot (\mu \nabla \vec{v}) \tag{3}$$

$$\nabla \cdot \left(\rho c_p \vec{v} T\right) = \nabla \cdot (k \nabla T) \tag{4}$$

where all the symbols are defined in the Nomenclature.

The heat conduction equation, given below, is solved in the solid substrate region, whereas the convective flow is considered in the channel.

$$\nabla \cdot (k \nabla T) = 0 \tag{5}$$

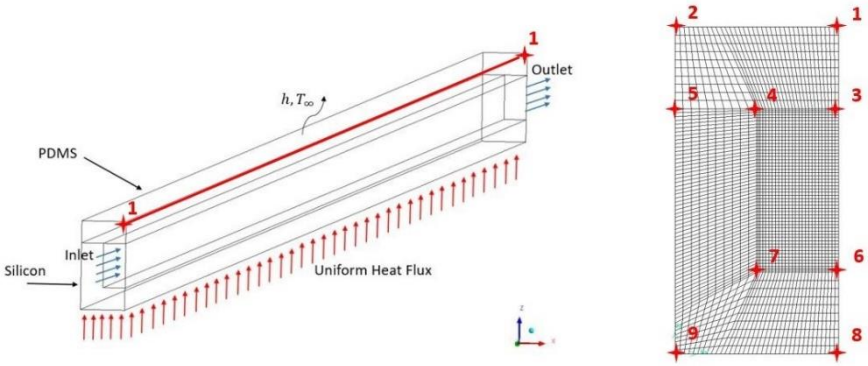

Figure 1 Model description and mesh generation for a single microchannel.

In this study, the boundary conditions used are as follows: (1) A uniform heat flux q'' is imposed at the bottom of the microchannel; (2) The velocity inlet and the pressure outflow are used at the entrance and exit, respectively; (3) To simulate the convection at

the top surface of the insulation layer, a constant heat loss coefficient is applied with its value estimated from the correlation in the equation given below[49]. The length scale used in the Nu and Ra calculation is $L_c = \frac{A_s}{P} = 0.0025\ m$.

$$Nu = 0.54Ra^{1/4} \tag{6}$$

The simulation results show that this natural convection heat loss is quite minor compared to the forced convection heat transfer through the microchannels.

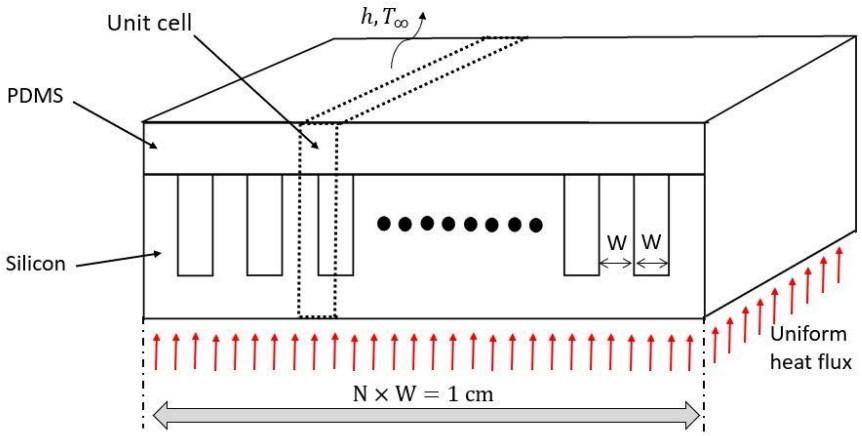

Figure 2 The unit-cell model description.

The optimization target is the 1cm by 1cm microchannel cooling system, and the simulation target is the unit-cell model. The details are illustrated in Figure 2. A small natural convection heat loss coefficient (h=15 W/m^2K) is applied at the top surface of PDMS insulation to simulate the natural convection heat loss on top. Grid independence is tested regarding the unit-cell model and a grid of larger than 580 K points are used for all cases.

Three design variables are considered in this work. The default value, design range, and uncertainty levels are listed in the table. The uncertainty from the number of channels

(channel width) is not considered in our study since its uncertainty is expected to be low in practical problems. Because we are considering a cooling system of 1cm by 1cm size, the number of channels has an inverse relation with the channel width. The relation is $N \cong 10^4/(2W)$.

Table 1 Design variables or operating conditions used.

Design variable or operating conditions	Unit	Default value	Design range	Uncertainty level
Flow rate	ml/min	-	0-250	5%
Heat flux	W/cm^2	50	20-80	5%
The number of channels	-	50	50-250	-

2.2 VALIDATION

An experimental setup was finished mainly for validation purposes. To further ensure simulation accuracy, the simulation results were compared with analytical calculations and the grid independence test was performed. Similar modelling approaches have been applied by other researchers [5]. To further validate the numerical model, some test simulations are carried out and the results are compared with the fully developed analytical results. Grid independence is tested in detail and a grid of larger than 580 K points are used for all cases. All solutions are converged to residuals lower than 10^{-6} for continuity/momentum and 10^{-9} for energy. These were varied to ensure that the results are independent of the chosen values.

2.2.1 Experimental comparisons

An open-loop experimental setup is built. The microchannels are fabricated through the wet etching technique. A syringe pump is used to provide water into the channels. The inlet/outlet pressure and temperature are measured with pressure transducers and water-proof thermocouples. The experimental circuit and the actual setup are shown in the figure.

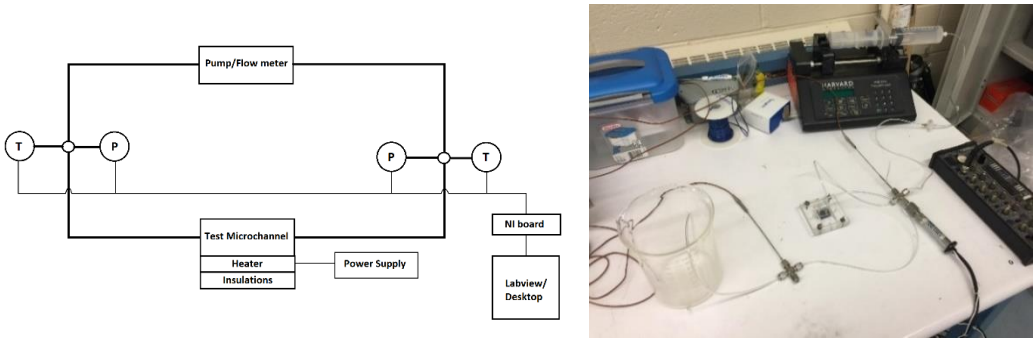

Figure 3 Experimental setup of the microchannel cooling system.

The pressure and temperature signals are collected using National instrument board and processed in the LabVIEW program. Heating power is supplied by a DC power supply and proper insulations are sealed.

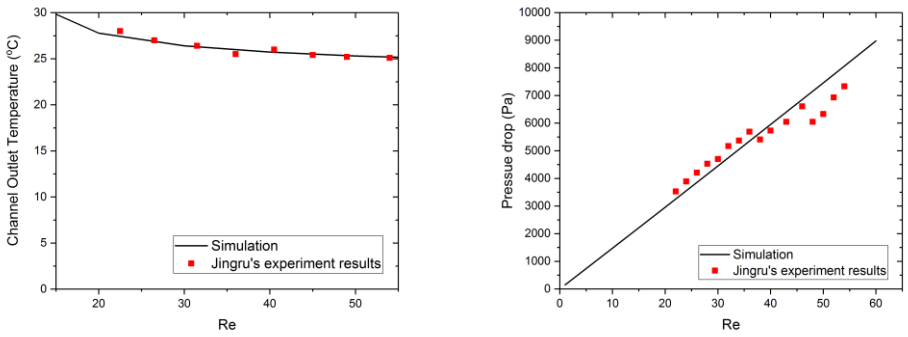

Figure 4 Temperature and pressure-drop comparisons between simulation and experiment.

In this comparison, a heat input of 2.4 W/cm^2 was applied at the substrate bottom. The channel outlet temperature and pressure drop across the channel are measured and simulated. The responses over a range of Reynolds numbers are compared. The channel outlet temperature decreases as the Reynolds number increases, and the pressure drop increases almost linearly in both simulation and experiments. A reasonably close match is observed in the figure shown.

2.2.2 Grid independence

First, five models with different grid sizes are built. Then, the same boundary conditions and solution methods are applied. Results such as pressure drop, fluid inlet/outlet temperature difference and hot-spot temperature are compared in Figure 5.

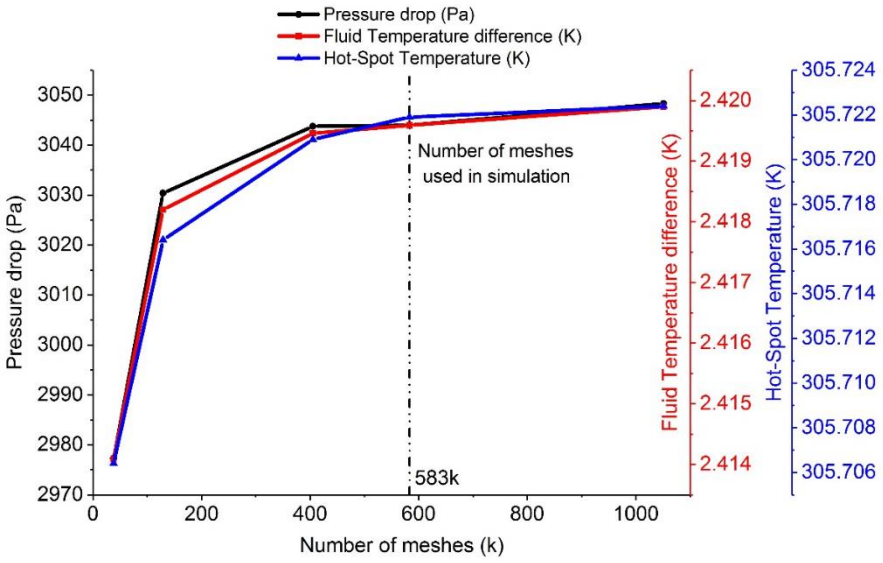

Figure 5 Grid Independence test under the conditions of $Re = 10$ and $q'' = 1\ W/cm^2$.

From this figure, we can see that the variations in the results are minor with mesh number of 583 K or higher. So, this grid is applied for all models.

2.2.3 Comparisons with analytical results

In the microchannel cooling setup, the incoming flow is in the developing phase in the entrance region. It gradually transforms into a developed flow. The pressure-drop within the developing phase is larger than the pressure-drop within the developed phase. In the developed phase, the numerically simulated simultaneously developing (SD) pressure-drop results should match with the analytically calculated fully developed (FD) results.

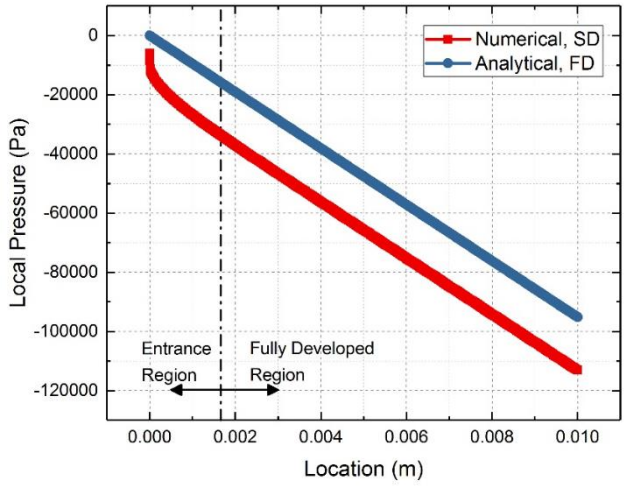

Figure 6 Local pressure comparison between simultaneously developing (SD) numerical simulation results and fully developed (FD) analytical results. Conditions: $N = 50, \dot{V} = 100\ ml/min.$

Even though simulations in this study are for developing cases, it isworthwhile to compare these numerical results with the fully developed analytical results. The main difference between developing and developed cases is the entry region. In the hydrodynamic entry region, the wall shear stress is very high, and the boundary thickness is comparatively small. Thus, the pressure gradient is highest at the inlet and decreases to a constant value when

the flow becomes fully developed. From Figure 6, the predictions based on theory are verified. This gives greater confidence in the numerical modelling.

2.3 MODELLING RESULTS

The numerical simulation results provide fundamental understanding on the microchannel-cooling system. Different design variables are tried. The main concentration is on the temperature and pressure-drop responses. Based on the modelling results, a better optimization formulation is achievable.

2.3.1 Temperature response

To obtain the hot-spot temperature locations, temperature plots along different locations are displayed in Figure 7. Traverses 1-9 are nine lines going from a location on the inlet plane to the corresponding ending location on the outlet plane. The 9 selected locations are listed here: (a) 2 traverses on the substrate bottom, (b) 2 traverses on the top surface of the insulation layer, (c) 1 traverse on the substrate/insulation interface, (d) 4 traverses on the four corners of fluid channel.

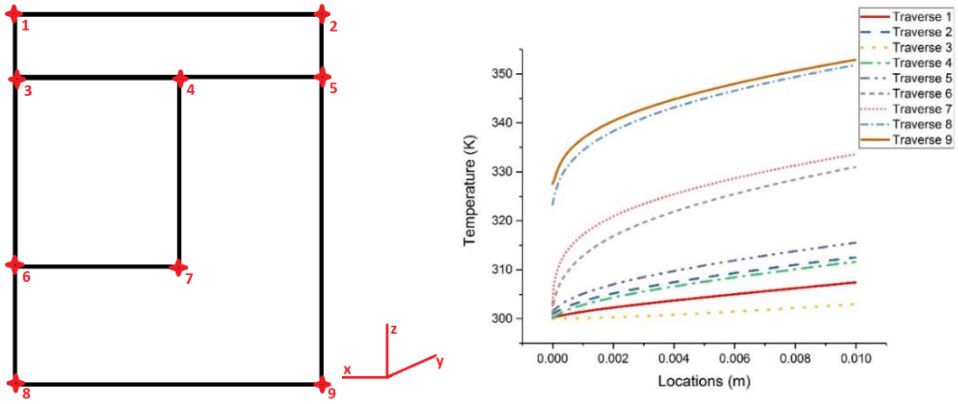

Figure 7 Temperature plots along different traverses.

This figure shows the temperature plots of simulation for the case of $N = 50, \dot{V} = 100\ ml/min$. In this study, a constant heat flux input is imposed at the bottom of the substrate.

The moving fluid inside the microchannel heats up as it removes the input heat. Thus, the channel serves as a heat sink. Temperature differences between heat source and heat sink are demonstrated in Figure 7. As the flow approaches the channel outlet, the fluid and substrate temperatures increase. All other cases have similar boundary conditions and thermal circumstances. Thus, the temperature plots behave similarly to Figure 7. The hot-spot temperature is observed to be always at the bottom of the outlet surface of the system and away from the fluid channel. In other words, for this geometry the hot-spot temperature consistently locates at the ending point of the traverse 9.

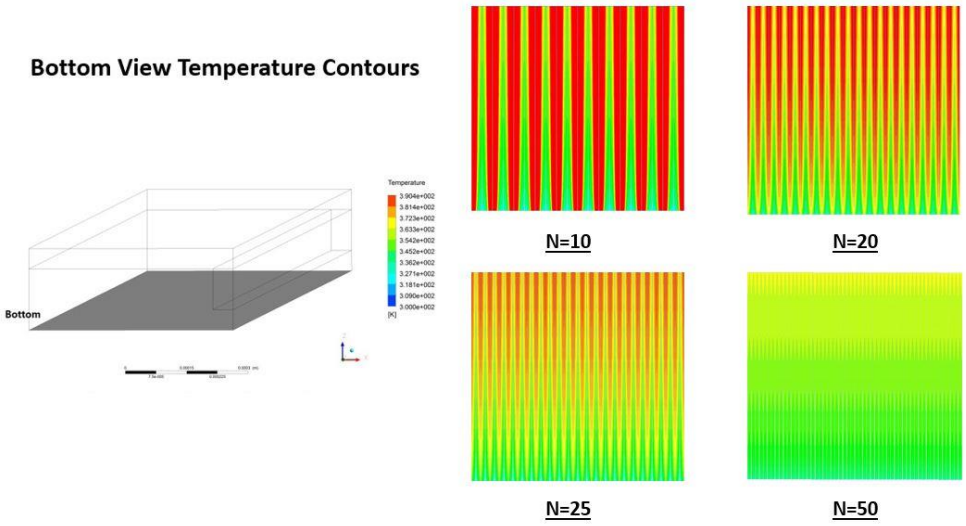

Figure 8 Bottom View Temperature Contours with different number of channels.

By changing the number of channels in the 1cm×1cm region, the system base temperature is illustrated in above figure. Microchannel system with more channel numbers shows better and more uniform temperature distribution. The hot-spot temperature is reduced from 640 K to around 356 K when the number of channels is increased from 10 to 50. Thus, increasing the number of channels can provide a much better thermal performance.

2.3.2 **Pressure-drop and pumping power responses**

With different incoming flow velocity, or Re, the responses from the pressure-drop, pumping power and system thermal resistance are displayed below. The pressure-drop across the channel is the inlet and outlet pressure difference across the entire channel. The pumping power can be calculated directly based on the pressure-drop and flow rate values. The system resistance is calculated based on the heat input and the averaged substrate temperature.

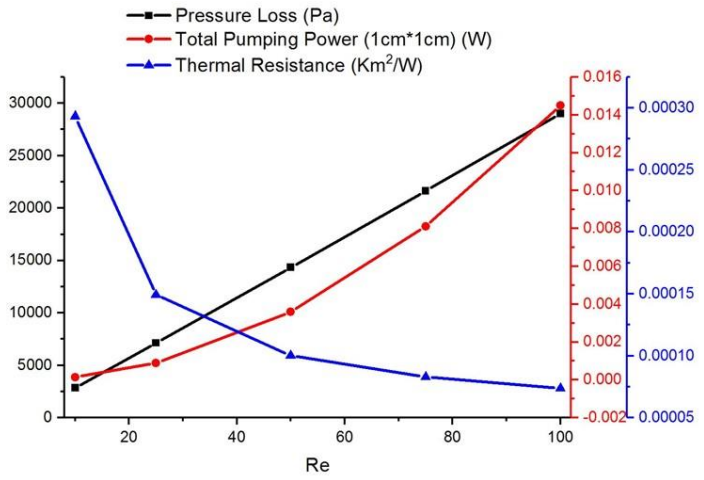

Figure 9 Pressure loss, total pumping power and thermal resistance responses with varying Reynolds number.

The thermal resistance reduces as the Reynolds number increases, which means a higher incoming flow benefits the system thermal performance as expected. However, the pressure-drop increases with the Reynolds number. Worse than that is the polynomial increasing pumping power. At lower Reynolds numbers, the thermal improvement is more significant, and the pumping power sacrifice is not that significant. At higher Reynolds numbers, the thermal improvement is much smaller, but the pumping power punishment

becomes quite high and non-negligible. This finding indicates that there might be an optimal Reynolds number or system design somewhere in the middle.

2.3.3 Cutoff flow rate and acceptable design region

If we define 'cutoff flow rate' as the flow rate above or below which the system will fail, it is possible to find a proper design region. In order to find the cutoff flow rate, we need the response plots with respect to the design variables. For the pressure-drop case, the cutoff flow rate is the design when the pressure-drop equals the pressure-drop constraint. The designs with higher flow rate will fail due to a unacceptable pressure-drop. For the temperature case, the cutoff flow rate is the design when the hot-spot temperature equals the temperature constraint. The designs with lower flow rate will fail due to the improper temperature.

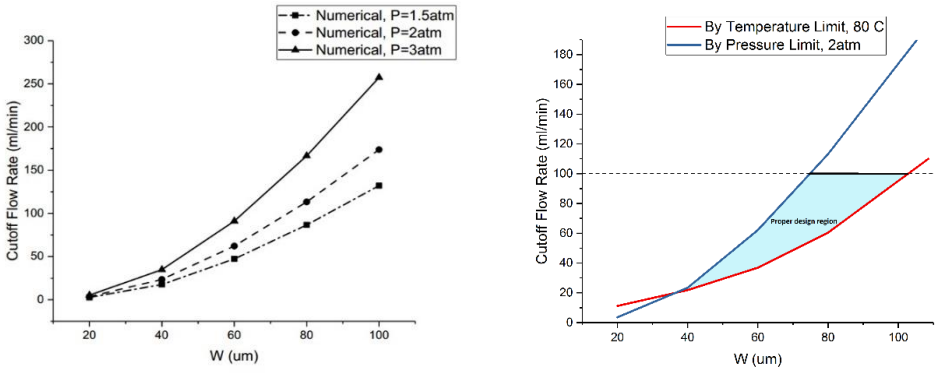

Figure 10 (Left) Cutoff flow rate for different pressure thresholds; (Right) Cutoff flow rate for $q'' = 50\ W/cm^2$.

Inside the proper design region, all designs are feasible. In other words, the pressure-drop does not exceed the pressure-drop limit value, and the hot-spot temperature is less than the temperature constraint. The fact is that the optimal design should be a design that lies inside the proper design region.

2.4 OTHER CHANNEL CONFIGURATIONS AND SUBSTRATE MATERIALS

Microchannel systems have many different configurations and material choices. The rectangular microchannel is the most common one due to its ease of fabrication. But it is not necessarily the best one for all applications. Circular and trapezoidal channels are some of the other geometry choices. Bifurcation, wavy, and oblique structures are some of the various heat enhancement structures available. Besides, the substrate material is another variable in designing a solid microchannel cooling system. All these different conditions will be reviewed in this section.

2.4.1 Circular

Microchannel geometries can be classified as circular and non-circular microchannels. In this study, we focus on rectangular microchannels, which is one type of non-circular channels. However, we cannot ignore the circular channels and its potential benefits. Particularly, some lab-on-chip applications require circular channels for special tasks such as cell growth. So, it is worthwhile to study the circular microchannels.

The flow areas are kept the same for both rectangular and circular configurations. With the same volume flow rates, the incoming velocities are the same for the two cases. The detailed arrangements are shown in the figure below:

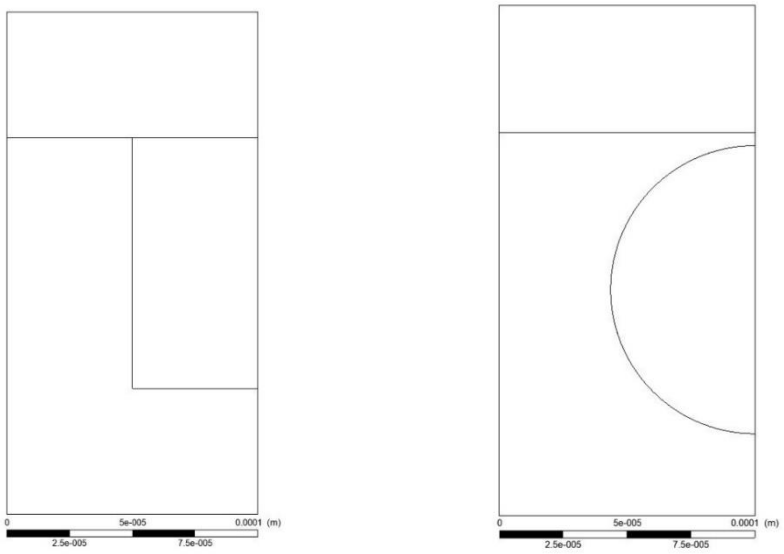

Figure 11 CAD details for (Left) the default rectangular design; (Right) the circular design.

A series of simulations are carried out accordingly. The flow rate is changed from 10 mL/min to 100 mL/min. The pressure-drop and hot-spot temperature results are compared.

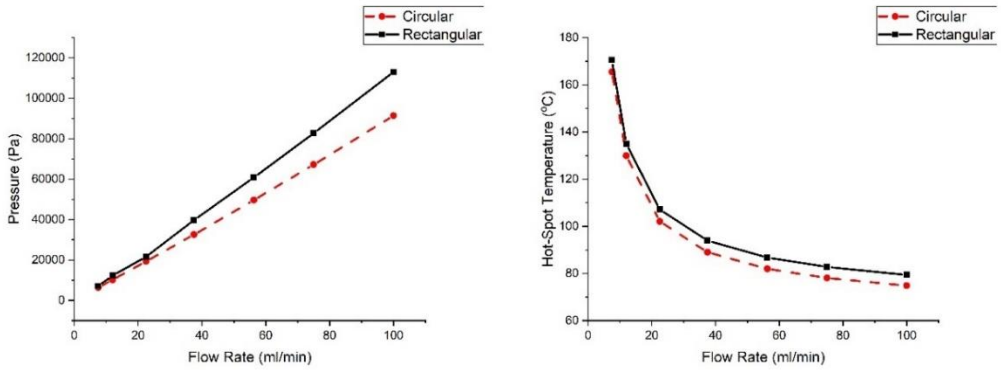

Figure 12 Pressure-drop and hot-spot temperature compares of the two designs.

From the above figure, the circular microchannel revealed better thermal and hydrodynamic performance. The circular channel pressure-drops are 5-20% less than the

pressure-drops of the rectangular channels. And the substrate temperature is also better controlled in the circular configuration.

2.4.2 Bifurcation

In the internal cooling systems, the developing flow region shows better heat transfer compared to the developed flow region. In the microchannel cooling system, the entrance region is small as the channel hydraulic diameter is small. To enhance the heat transfer, one natural way is to add bifurcation regions when the flow becomes developed. The design, together with its computational domain, is shown in below figure.

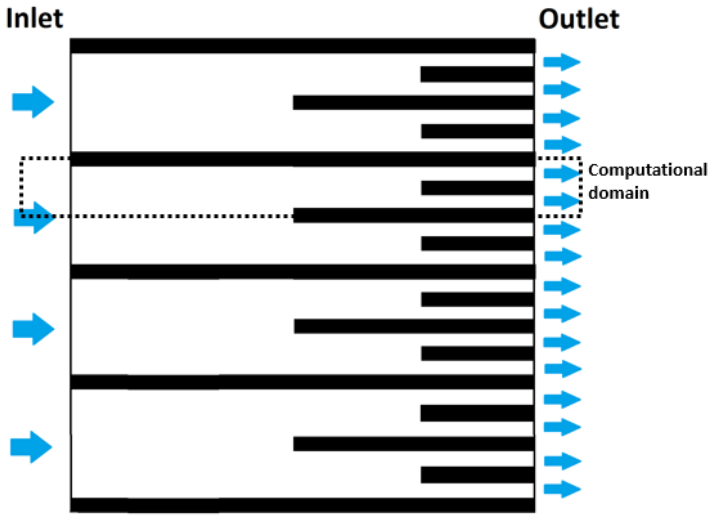

Figure 13 Graphic representation of a bifurcation design.

When an additional partition is added in the tunnel, there are two mechanisms that enhanced the heat transfer in the bifurcation design. One enhancement comes from the flow pattern as the flow is transferred from developed flow to developing flow. When the bifurcation occurs, the microchannel width is reduced by half. And the heat transfer for smaller diameter channels will be improved accordingly.

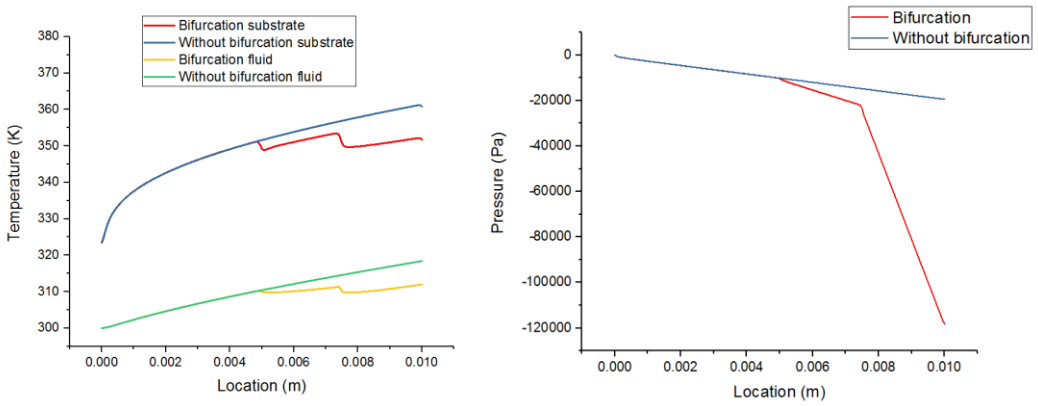

Figure 14 Comparison between bifurcation model and original model without bifurcation: (Left) Temperature, (Right) Pressure.

The above figure shows the temperature and pressure-drop comparisons. Compared to the logarithmic increasing substrate temperature of the original design, the substrate temperature of the bifurcation design is a lot more uniform. This can help reduce the hot-spot temperature and the thermal resistance of the cooling system. Unfortunately, the pressure-drop is much higher compared to the original design.

We also tested other heat enhancement methods such as wavy structure, channel with baffles, and converging-diverging channels. The thermal improvement is always accompanied with higher hydrodynamic punishment. For example, all these heat enhancement methods reduce the hot-spot temperature and thermal resistance. But at the same time, the pressure-drop increases. Most available heat enhancement methods are employed to break the developed flow into developing flow. The developing flow region has a higher pressure-drop gradient compared to developed flows.

2.4.3 Mini-channels

Mini-channels are capable of handling large heat flux as well. Generally, channels with sizes larger than 0.5 mm can be treated as mini-channels. For mini-channels, the

required pressure-drop is much smaller. Some cooling applications do not generate large heat flux. And the mini-channel device is a good option which balances both thermal requirement and pumping demand.

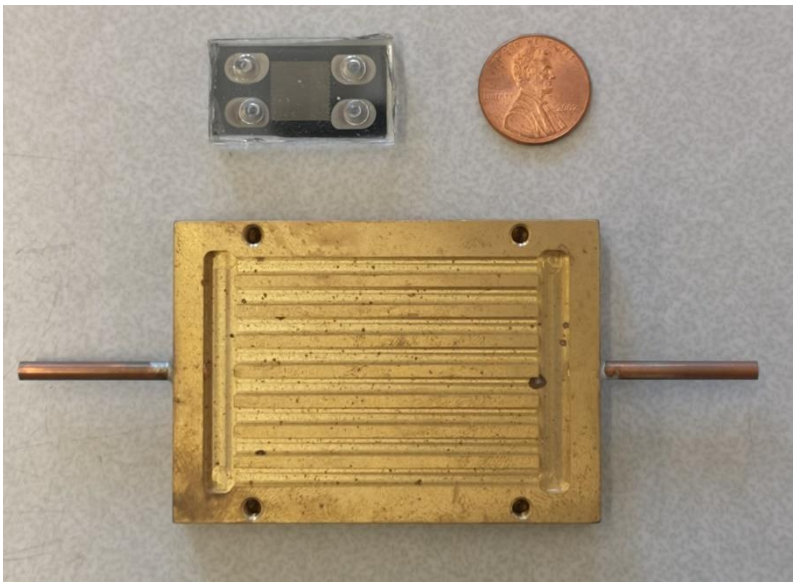

Figure 15 A comparison of a microchannel device with a mini-channel device.

The home-made microchannel and mini-channel devices are shown in the figure above. The fabrication of mini-channel device can be easily done by computer numerical control (CNC) machines. This ease of fabrication is another attractive advantage of mini-channels.

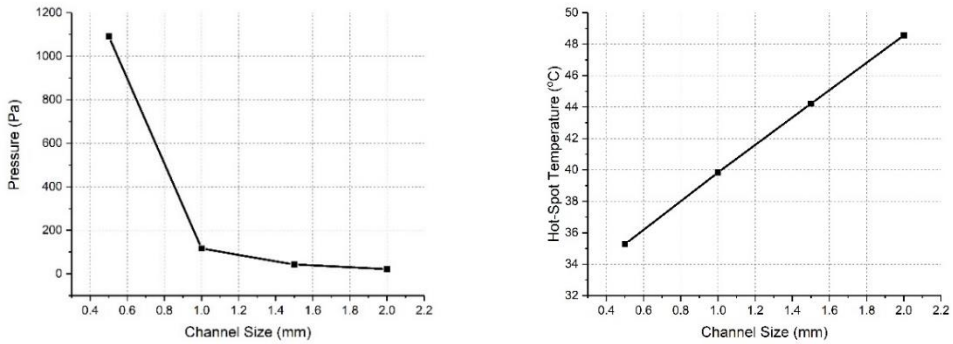

Figure 16 Pressure-drop and hot-spot temperature variations with channel size, $q'' = 10{,}000\ W/m^2$.

The pressure-drop and temperature variations with the channel size are shown. Like what is observed in the microchannels, the pressure-drop decreases exponentially as the channel size increases, while the temperature has a positive linear relation with the channel size. But the pressure-drop magnitude (kilo-pascal range) is much smaller compared to the ones in microchannels (10^5-pascal range).

2.4.4 Different substrate materials

In the electronic cooling applications, some of the choice substrate materials are silicon, aluminum, cooper, Silicon carbide (SiC), bronze, and diamond. In this study, the default substrate material is silicon. Compared to the silicon thermal conductivity of 1.3 W/mK, bronze has a thermal conductivity about 20 times higher. The simulation results are shown.

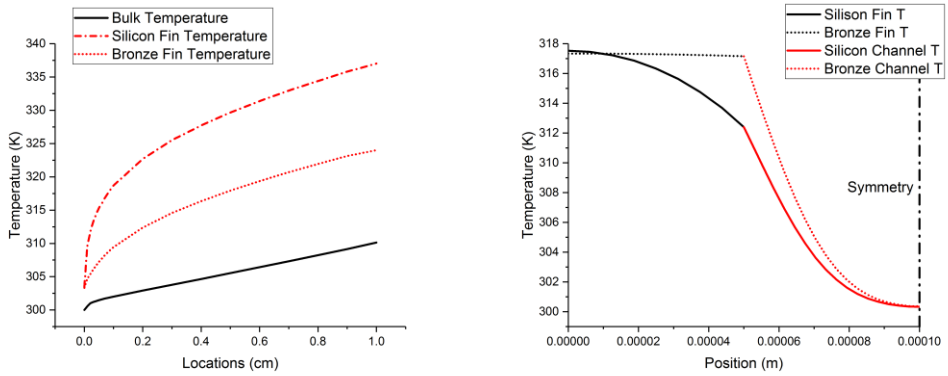

Figure 17 Microchannel temperature comparisons with silicon substrate and bronze substrate.

The pressure-drop between the two cases are the same. However, the substrate temperature distributions differ a lot. The figure above is the temperature plot comparison for two different substrate materials: Bronze and Silicon. The temperature gradient for bronze-made substrate is much lower compared to the temperature gradient for silicon-made substrate. This is due to the higher thermal conductivity of bronze. For the same reason, the average temperature for bronze-substrate is lower than silicon-substrate. To control the hot-spot temperature, one desirable way is to replace the substrate material to a higher conductive one.

2.5 BIO-ENGINEERING APPLICATIONS

Besides the electronic cooling application, microchannel flows show great potential in bio-technologies. One example is microfluidics devices. With the micro-scale devices, low sample consumption, shorten experimental time, and better experimental accuracy are possible. However, thermal effects on bio-engineering microchannel applications have barely been studied.

Blood vessels have a wide range of dimensions. The dimensions of aorta, artery, arterioles, terminal arterioles, and capillary are approximately 25 mm, 4 mm, 30 μm, 10 μm, and 8 μm [50]. The human blood flows are transition flows from mini-channel to microchannel.

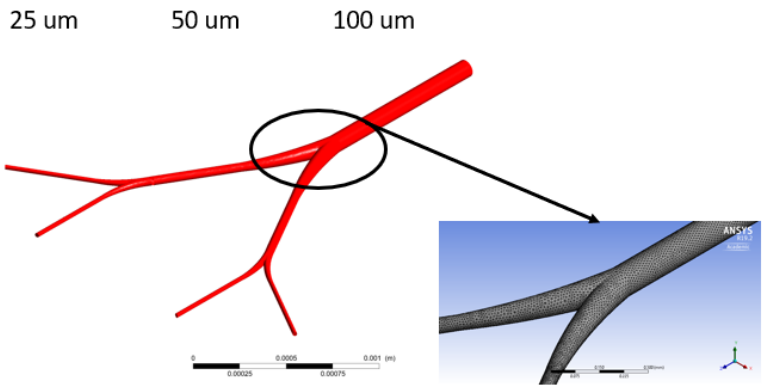

Figure 18 3D CAD geometry for simulated blood vessels.

A short piece of blood vessel transition from 100 μm to 25 μm is numerically simulated. This could be a bifurcation session of artery to arterioles.

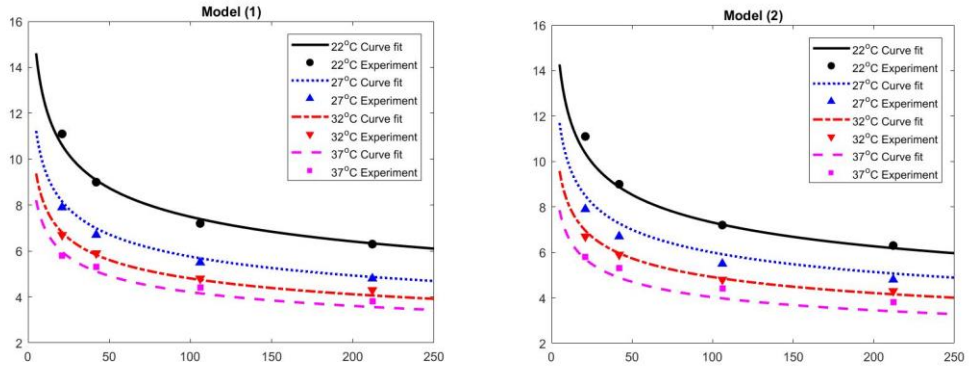

Figure 19 Blood viscosity models (1) & (2).

The blood viscosity is dependent on both temperature and shear rate. To better approximate the viscosity, two different viscosity models are compared.

Model (1):

$$\mu = k\dot{\gamma}^{n-1} exp[\alpha(\frac{1}{T} - \frac{1}{T_{ref}})] \quad (7)$$

Model (2):

$$\mu = k\dot{\gamma}^{n-1} exp[\alpha(T - T_{ref})] \quad (8)$$

The blood viscosity data set is collected from Rand et al. [51]. In this paper, they measured the viscosity at various levels of hematocrit, temperature and shear rate. The data set at 40 Hct is used. The comparisons and error estimations are shown in the figure above and the table below. Model (2) provides lower errors and better accuracy, and it is chosen as the viscosity model.

Table 2 Two fit model of the Blood Viscosity relations with Temperature/shear rate.

Short name	Description	Model (1)	Model (2)
sse	Sum of squares due to error	0.7279	2.1139
rsquare	R-squared (coefficient of determination)	0.9866	0.9611
rmse	Root mean squared error (standard error)	0.2366	0.4032

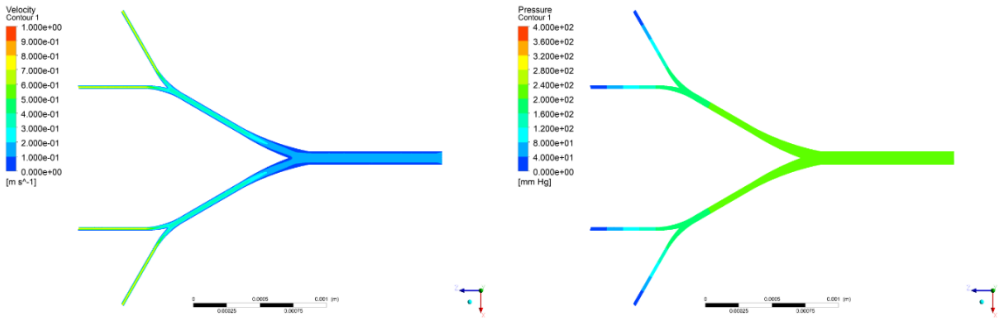

Figure 20 (left) Velocity contours with power law viscosity; (right) Pressure contours with power law viscosity.

In this simulation, the inlet boundary condition is a constant velocity, the outlet is a pressure-outlet. All vessel walls are taken as adiabatic. In future studies, thermal boundaries can be applied on the walls. The thermal and pressure responses of blood flow under constant heat flux and constant temperature cases can be studied.

Figure 20 shows the velocity and pressure contours of the blood vessels. A pressure drop of about 300 mmHg is required to drive the blood motion at 0.1 m/s through the 3 mm distance.

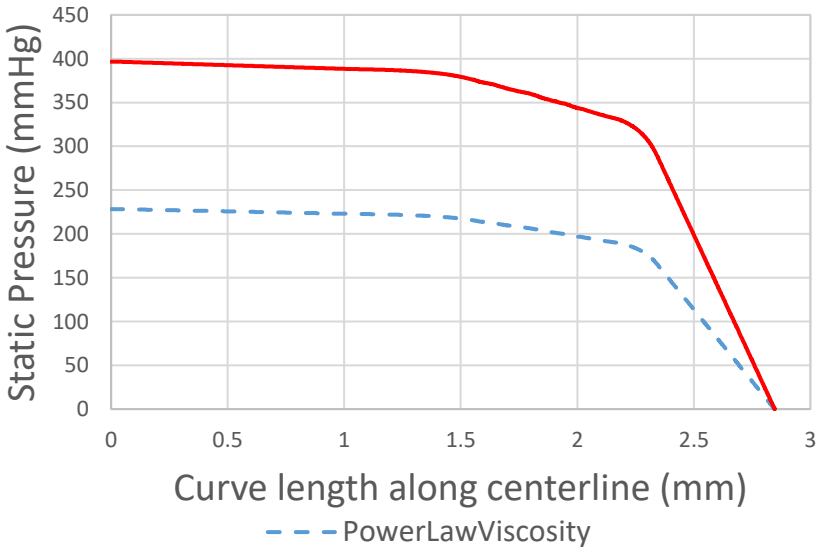

Figure 21 Local static pressure along vessel centerline with compares of (1) constant viscosity and (2) power law viscosity.

The pressure plot along the vessel centerline is shown in the figure above. The pressure drop gradient is small in the artery region and large in the arteriole region. This trend matches well with the experimental results of Zweifach [52].

3 DETERMINISTIC OPTIMIZATION OF MICROCHANNEL COOLING SYSTEMS

The pressure, temperature, pumping power and thermal resistance of the system were calculated based on the unit modelling results. Two practical concerns, the pressure drop limitation and the hot-spot temperature limitation, were taken as constraints. Beyond certain limits that are pre-determined, the system will fail, and the design becomes infeasible.

3.1 PRACTICAL LIMITATIONS

The microchannel heat removal system is usually applied to cool electronic devices. The heat flux could be very high, sometimes up to $100\ W/cm^2$. In this work, the heat flux is in the range of $20 - 60\ W/cm^2$, which is about 200-600 times direct solar radiation. In such a small area, the existence of this large heat input will accompany unacceptable joint temperatures if not being cooled properly. Even though the microchannel cooling technique is employed, the joint temperature may still shoot up to 90 ℃ or higher.

For microchannel cooling systems, the pressure drop can easily reach 1 atmosphere. To further reduce the hot-spot temperature, a better cooling performance is desired which means higher flow rates or smaller channel dimensions. Both approaches engender even higher pressure drops. On the other hand, pumps that have a comparable size can hardly provide pressure drops higher than 1 atmosphere. The micro-pumps can be categorized into two large branches: Mechanical displacement driven and Electro- and Magneto-kinetic driven. Mechanical driven pumps include diaphragm, rotary and phase change pumps. Electro and Magneto-kinetic consist of electrodynamic, electroosmotic, electrowetting and magnetohydrodynamic [13]. The size of micro pumps is at micro level but they can barely handle enough flow rate for cooling purposes. The industrial pumps can afford both high

pressure and enough flow rate but their sizes are relatively large. Also, the silicon substrate may fail due to the accompanied high mechanical stress. Summarizing both situations, the pressure drop constraint is taken as 3 atmospheres in this work.

3.2 PARAMETRIC MODELLING

There are two conflicting objectives, pumping power and thermal resistance in this scenario. The goal is to control the objectives below specified acceptable limits. In this work, two sets of design variables are evaluated: (Set I) Incoming flow rate and number of channels; (Set II) Incoming flow rate and heat flux. To represent the thermal and fluid behavior in terms of design variables, Polynomial Response Surface (PRS) methodology is used. Referring to the available optimization procedures [53], appropriate formulations of the microchannel cooling system are constructed. For improved thermal performance, one objective is to minimize the thermal resistance. Another objective is to minimize the pumping power. Pressure drop and hot-spot temperature constitute two major design constraints. Subsequently, a more practical multi-objective optimization problem is formulated instead of optimizing the pumping power and thermal resistance individually. Lastly, a Pareto frontier optimization is performed using a similar approach for both cases.

Based on the simulation results, performance response curves are formulated for hot-spot temperature, pressure, thermal resistance and pumping power. Hot-spot temperature and pressure data points can be obtained from the simulation results directly while pumping power and thermal resistance have to be calculated through the two equations given below [48, 49]. This process leads to four curve-fitted functions for (Set I) and (Set II) each. From the fully developed flow analysis, the four responses can be roughly

estimated by polynomial combinations of the two sets of design variables [48, 49, 54]. So the most common and straightforward Response Surface Method (RSM) tool, PRS, is used.

$$Power = \frac{\dot{m}\Delta p}{\rho} \tag{9}$$

$$\theta = \frac{T_{sub,avg} - T_{in}}{q''} \tag{10}$$

The exact form of the PRS used is:

$$F(x, y) = p_{00} + p_{10}x + p_{01}y + p_{20}x^2 + p_{11}xy + p_{02}y^2 \tag{11}$$

For (Set I), The design variables are flow rate $\dot{V}$ (or the inverse of $\dot{V}$) and number of channels N (or the inverse of N). The number of channels N has inverse relation with the channel width, thus being $N \cong 10^4/(2W)$. For (Set II), The design variables are flow rate $\dot{V}$ (or the inverse of $\dot{V}$) and heat flux q''. The choice is made based on the analytically derived equations. For example, the pressure-drop equation for internal laminar flow can be written as $\Delta P = f\frac{L}{D}\frac{\rho V_{avg}{}^2}{2}$. Average velocity has a positive relation with the flow rate. Thus, the flow rate $\dot{V}$ and the inverse of channel width $1/W$ (the number of channels) are used as the variable x and y in the pressure-drop parametric modelling. A quick summary of the PRS arguments and coefficients calculated are shown in Table 3 and Table 4.

3.2.1 Flow rate and channel width

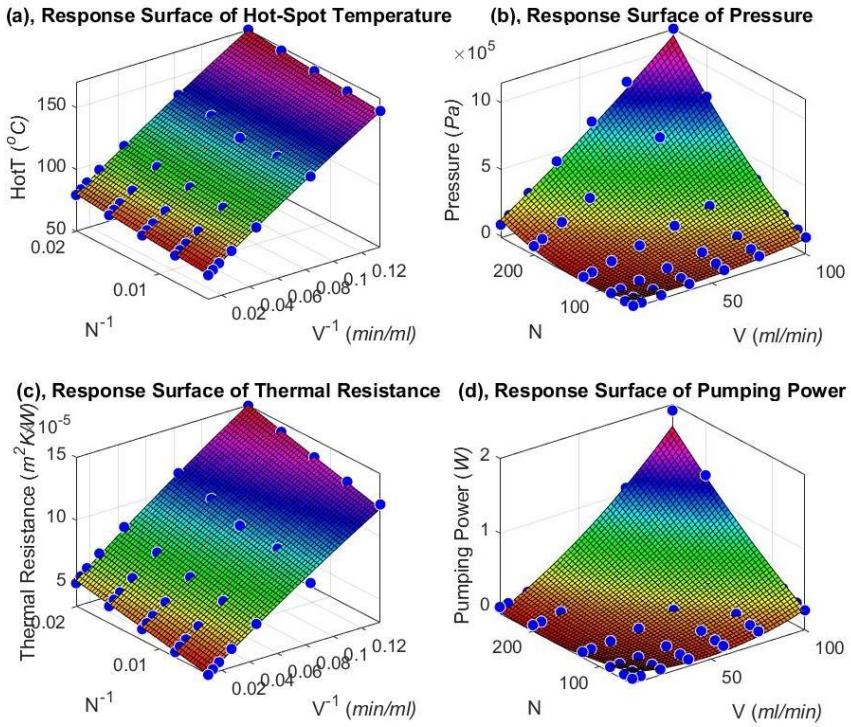

Figure 22 Response surfaces of (Set I) for hot-spot temperature, pressure drop, thermal resistance and pumping power.

Table 3 Polynomial curve fitting details of (Set II).

Case	x	y	p_{00}	p_{10}	p_{01}	p_{20}	p_{11}	p_{02}
Hot-Spot Temperature	$\dot{V}^{-1}$	q''	60.46	309.2	392.4	-582.9	360.8	9324
Thermal Resistance	$\dot{V}^{-1}$	q''	1.902e-05	0.000906 7	0.000866 1	-0.001153	0.002409	0.01482
Pressure	$\dot{V}$	q''	1.335e+05	-2214	-2464	0.8879	52.76	8.045
Pumping Power	$\dot{V}$	q''	0.3456	-0.01088	0.004519	6.58e-05	9.439e-05	9.332e-06

In this study, 6 different flow rates and 5 different number of channels or 5 different heat flux values are selected and simulated. In total, there are $6 \times 5 \times 5$ simulation data points. The polynomial response surfaces are shown in Figure 22 and Figure 23.

3.2.2 Flow rate and heat input

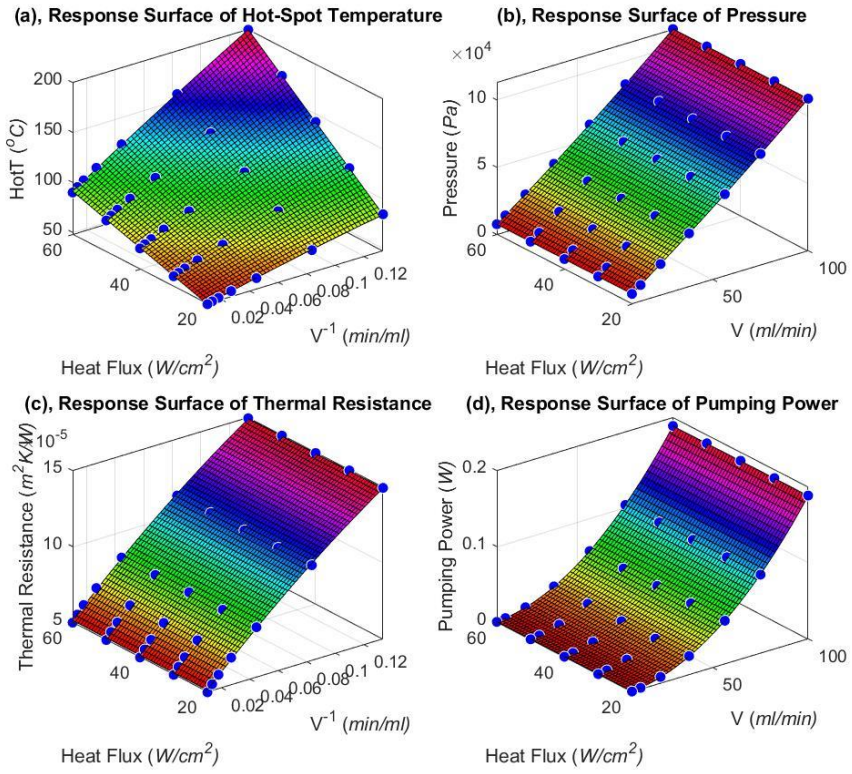

Figure 23 Response surfaces of (Set II) for hot-spot temperature, pressure drop, thermal resistance and pumping power.

In these figures, the x and y axis represent the design variables. The fitted results are shown on the z axis. The numerical results are shown as the blue dots while the surfaces are the fitted functions. The R squared value as correlation coefficients, for the response surfaces are above 0.95. Thus, good matches are obtained.

Table 4 Polynomial curve fitting details of (Set II).

Case	x	y	p_{00}	p_{10}	p_{01}	p_{20}	p_{11}	p_{02}
Hot-Spot Temperature	$\dot{V}^{-1}$	q''	25.83	59.24	0.7764	-401.5	14.5	-1.19e-08
Thermal Resistance	$\dot{V}^{-1}$	q''	2.77e-5	0.0008803	-1.562e-21	-0.0008647	1.531e-20	1.479e-23
Pressure	$\dot{V}$	q''	-61.99	3399	-5.116e-10	0.9077	-1.782e-11	2.396e-08
Pumping Power	$\dot{V}$	q''	0.0009676	-0.0001054	-1.208e-14	5.908e-05	-6.796e-18	1.828e-13

From Figure 22, thermal resistance and hot-spot temperature responses decrease as flow rate and number of channels increase. On the contrary, pressure and pumping power responses increase as flow rate and number of channels increase. Flow rate effects are the same in Figure 22 and Figure 23. From Figure 23, only the hot-spot temperature is dependent on the heat flux input variable. As the flow rate and number of channels increases, the heat transfer is enhanced due to a higher heat transfer coefficient and larger contact area. But the required pressure-drop will be increased as pumping more water through smaller channels requires higher pressure-drop.

3.2.3 Response surfaces based on Radial basis function (RBF)

The RBF is a series of the chosen basis functions. The general form is the equation below [55].

$$f(x) = \sum_{i=1}^{N} w_i \varphi(\|x - x_i\|) \tag{12}$$

In this equation, f is the response, and x is the input. The basis function is $\varphi(\|x - x_i\|)$, and w_i is the weighting factor of each basis function for the ith input. In our case, the modified form of Euclidean distance is used as the basis function. So, the general form can be rewritten as the following:

$$f(x) = \sum_{i=1}^{N} w_i \sqrt{\left(\frac{x-x_i}{x_m}\right)^2 + \left(\frac{y-y_i}{y_m}\right)^2} \tag{13}$$

Polynomial function is easy, but it has large fitting errors when the response surfaces have distinct local behavior. On the other hand, RBF goes through all input pairs. It has much higher accuracy in the estimations of local response surfaces. We will illustrate this point in the CVD applications.

3.3 SINGLE- AND MULTI- OBJECTIVE OPTIMIZATION

3.3.1 Single-objective optimization

The goal of single-objective optimization is to minimize or maximize a certain objective function under proper constraints. As mentioned earlier, the objective functions are thermal resistance and pumping power, which are calculated from the equations in section 3.1.

The first formulation is to minimize the non-dimensional thermal resistance, while satisfying the pressure and temperature constraints. This aims at reaching better cooling performance without consideration of pumping power.

$$\begin{aligned} Min_{Q,N} \quad & \frac{\theta}{|\theta_{max}|} \\ s.t. \quad & Pressure \leq 3\ atm \\ & HotT \leq 90℃ \\ & 5 \leq \dot{V} \leq 100\ ml/min \\ & 50 \leq N \leq 250 \end{aligned} \tag{14}$$

With the existence of the pressure and temperature constraints, the feasible solution should stay to the left of the pressure constraint line (blue) and to the right of the temperature constraint line (red). On the left side of the pressure constraint, the design has a low number of channels and flow rate. The pressure-drop does not exceed the pressure-drop constraint. On the right-side of the temperature constraint, the design has a high

number of channels and flow rate. The hot-spot temperature does not exceed the hot-spot temperature constraint.

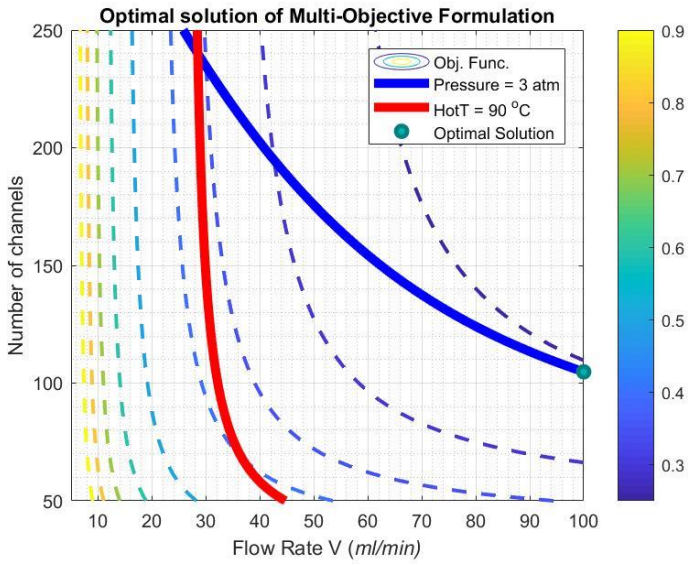

Figure 24 Optimal solution for minimizing the thermal resistance.

From Figure 23 (c), higher flow rate and a larger number of channels are required to reduce the thermal resistance. Thus, this optimization leads to an optimal point close to the pressure constraint boundary with maximum allowed flow rate. The optimal point in design variable plane is shown as a green dot in Figure 24. To minimize the thermal resistance, the design with highest allowed flow rate and number of channels is selected. This design provides the best thermal performance within the feasible design domain.

The second formulation is to minimize the non-dimensional pumping power, while satisfying the pressure and temperature constraints. The target is to reduce the required pumping power without system failure.

$$Min_{Q,N} \quad \frac{Power}{|Power_{max}|}$$

$$s.t. \quad \begin{array}{c} Pressure \leq 3\ atm \\ HotT \leq 90℃ \\ 5 \leq \dot{V} \leq 100\ ml/min \\ 50 \leq N \leq 250 \end{array} \tag{15}$$

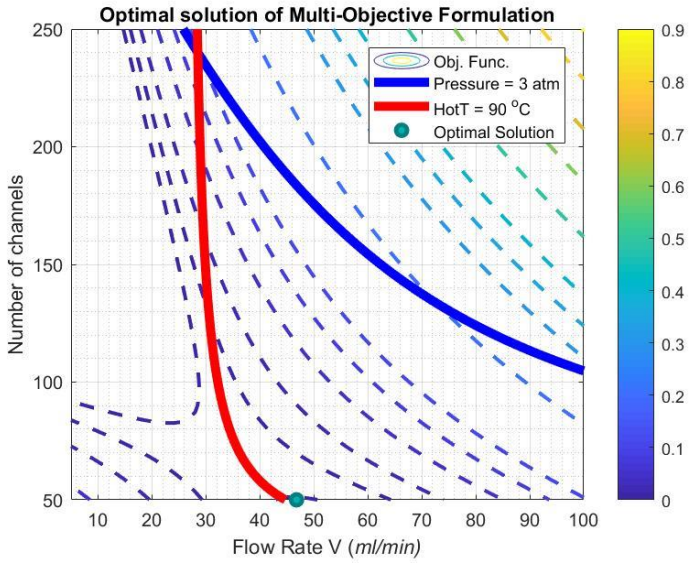

Figure 25 Optimal solution for minimizing the pumping power.

From Figure 23 (d), lower flow rate and smaller number of channels are needed to lower the pumping power. Contrary to minimizing the thermal resistance, it can be expected that the optimal solution for minimizing the pumping power should yield either smallest flow rate or smallest number of channels in the feasible region. The number of channels has inverse relation with the channel width, and the channel width has a close relation with the hydraulic diameter D_h of the channels. Compared to flow rate $\dot{V}$, hydraulic diameter D_h has higher influence on the pumping power. Thus, this optimization leads to an optimal point close to the temperature constraint boundary with minimum allowed number of channels. The optimization result is shown as a green dot in Figure 25.

3.3.2 Multi-objective optimization

The third formulation is to minimize the non-dimensional thermal resistance and the non-dimensional pumping power within the feasible design domain. A linear summation with equal weights on each function is applied. The detailed formulation is in below equation.

$$\begin{aligned} Min_{Q,N} \quad & \frac{\theta}{|\theta_{max}|} + \frac{Power}{|Power_{max}|} \\ s.t. \quad & Pressure \leq 3\ atm \\ & HotT \leq 90℃ \\ & 5 \leq \dot{V} \leq 100\ ml/min \\ & 50 \leq N \leq 250 \end{aligned} \tag{16}$$

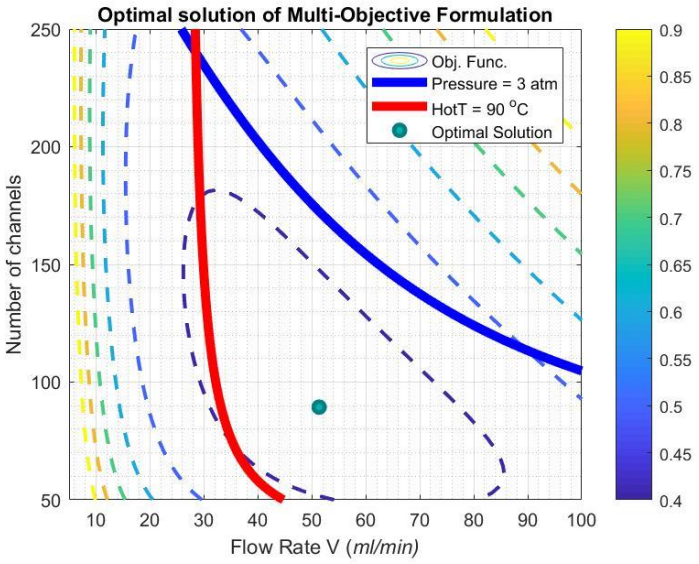

Figure 26 Optimal solution of the multi-objective optimization problem, considering the effects of both the pumping power and the thermal resistance.

The feasibility and the optimal solution are shown in Figure 26, where the optimal point is shown as a green dot. This solution provides a balanced solution between thermal resistance and pumping power. With equal weights on thermal resistance and pumping

power, there are no alternate solutions that yield better performance under the given constraints.

3.3.3 Pareto Frontiers

Pareto optimality is a solution that cannot be improved in one objective without making another one worse off. A series of Pareto optimal solutions are called Pareto frontiers. In order to calculate the Pareto frontiers, linearly varying weights ω and $1-\omega$, instead of equal weight, are used in the formulations. Thus, the single- and multi-objective optimization discussed above are merely special cases of Pareto optimization. When $\omega = 1$, the optimization is exactly the single-objective optimization for minimization of the thermal resistance. When $\omega = 0$, the optimization is exactly the single-objective optimization for minimization of the pumping power. When $\omega = 0.5$, the optimization is exactly the multi-objective optimization in section 3.3. For this reason, the single- and multi- optimization for (Set II) are already included in the Pareto frontiers of this section. The Pareto optimization formulations are shown in below equation.

$$
\begin{aligned}
Min_{Q,N} \quad & \omega \frac{\theta}{|\theta_{max}|} + (1-\omega)\frac{Power}{|Power_{max}|} \\
s.t. \quad & Pressure \le 3\ atm \\
& HotT \le 90℃ \\
& 5 \le \dot{V} \le 100\ ml/min \\
& (Set\ I)\ 50 \le N \le 250\ \ or\ (Set\ II)\ 20 \le q'' \le 60\ W/cm^2 \\
& 0 \le \omega \le 1
\end{aligned}
\tag{17}
$$

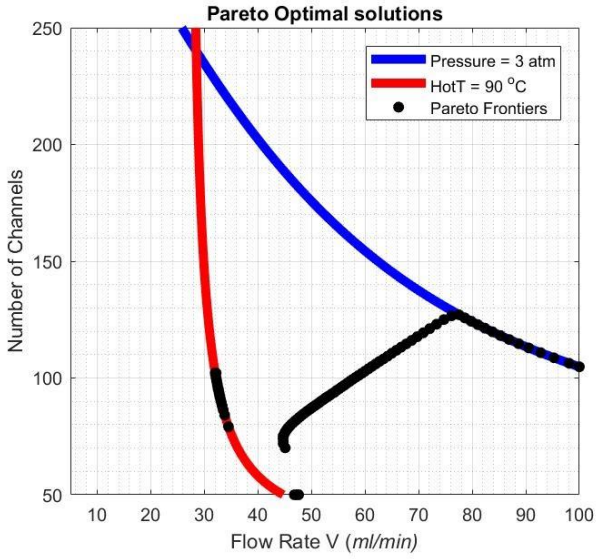

Figure 27 Pareto frontiers for (Set I) at constant heat flux $q'' = 50\ W/cm^2$ in the design variable plane.

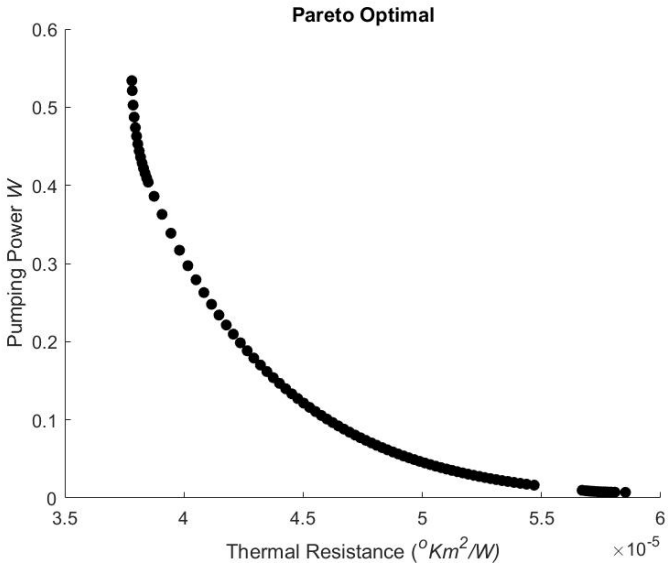

Figure 28 Pareto frontiers for (Set I) at constant heat flux $q'' = 50\ W/cm^2$ in the objective plane.

For (Set I), Pareto frontiers are shown in two different views. From the design variable plane in Figure 27, with a weight around 0, Pareto frontiers lie close to the

temperature constraint while a weight around 1 produces Pareto frontiers close to the pressure constraint.

In the objective plane of Figure 28, Pareto frontiers form a smooth curve from left top corner to right bottom corner. The entire feasible domain lies above this curve while the cases below this curve all fail due to either a high pressure drop or a high hot-spot temperature. Thus, Pareto frontier curves give guidance on future designs. If a lower thermal resistance is required without any risk of system failure, a higher pumping power is necessary. More specifically, the supplied pumping power should be no less than the pumping power of the corresponding Pareto frontier point. For example, if a thermal resistance less than $4 \times 10^{-5}\ °Km^2/W$ is needed, then the pumping power will be higher than 0.3 W.

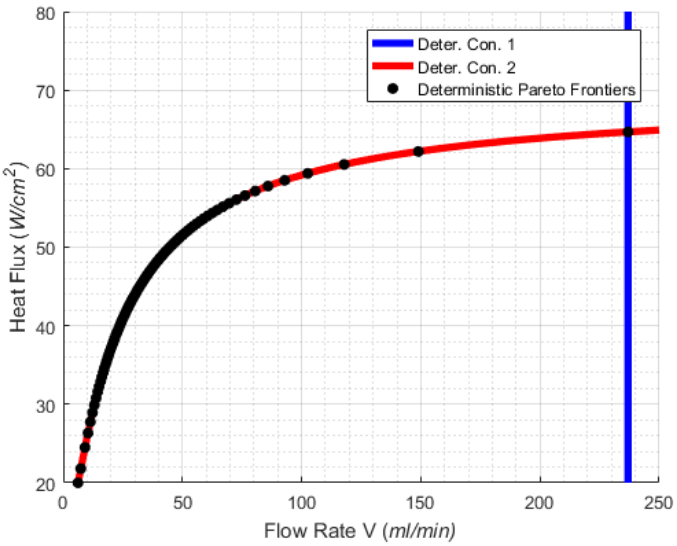

Figure 29 Pareto frontiers for (Set II) at constant number of channels $N = 50$ in the design variable plane.

For (Set II), the solutions are shown in Figure 29. Pareto frontiers for this case are fairly elementary points on the Hot-Spot temperature constraints. This is because the two

objectives: thermal resistance and pumping power are both independent of the design variable heat flux. The solutions that provide maximum heat flux inputs are obtained as the optimal solutions. To do so, a very minor adjustment term is applied to the objective function. Those solutions are exactly the points on the temperature constraint. From Figure 29, the maximum heat flux in the feasible design domain is 64.67 W/cm^2.

The Pareto frontiers for (Set II) are under constant number of channels $N = 50$. If we change number of channels and repeat the Pareto optimization process of (Set II). Different maximum feasible heat flux under 5 different geometries can be obtained. The results are shown in Figure 30.

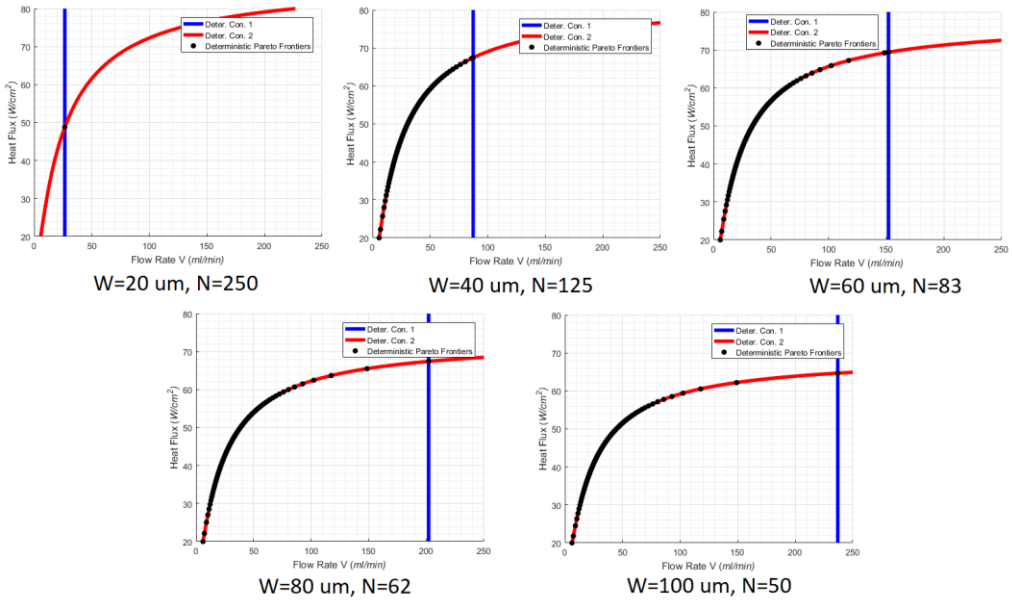

Figure 30 Pareto frontiers for (Set II) with different number of channels $N = 50, 62, 83, 125, 250$.

With a larger number of channels, the hot-spot temperature constraint curve (red curve) moves towards higher heat flux. This means the thermal performance is better without the consideration of pressure drop. But the pressure-drop constraint curve (blue

curve) moves very quickly towards the smaller flow rate direction. With a total flow rate less than 30 ml/min, system design with $W = 20\ \mu m$ and $N = 50$ can hardly remove heat flux of $50\ W/cm^2$. This value is the least feasible heat flux among the five designs.

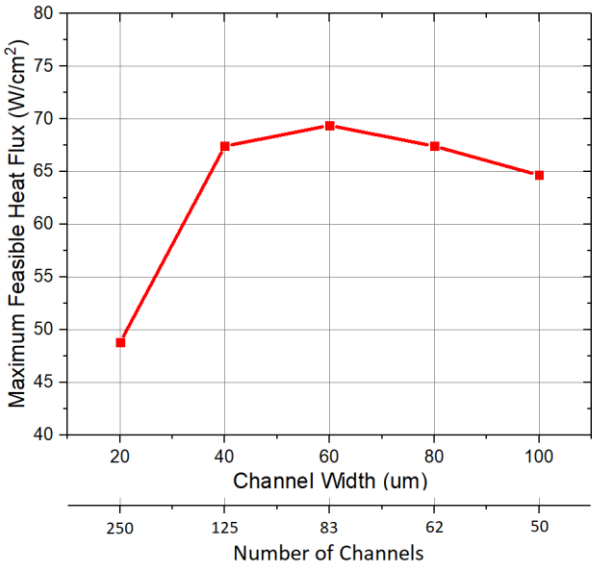

Figure 31 Optimal channel configuration.

In Figure 31, a maximum feasible heat flux 69.39 W/cm^2 exists when number of channels N equals 83 or channel width W equals $60\ \mu m$. For designs with a larger number of channels or a smaller number of channels, the maximum feasible heat flux will be lower. For more channels or smaller channel widths, the pressure drop serves as the primary limitation of the maximum allowable heat flux. On the contrary, the hot-spot temperature serves as the primary limitation for a smaller number of channels or larger channel widths. Without system failure, this geometry with number of channels N equals 83 can remove the maximum heat flux. It is the optimal channel geometry in this study.

To remove higher heat flux than 69.39 W/cm^2, either a higher pressure drop limitation beyond 3 atm or higher hot-spot temperature limitation beyond 90 ℃ is required.

However, a pressure drop of 3 atm and hot-spot temperature of 90 ℃ are common and realistic design limits for electronic systems [3].

4 RELIABILITY-BASED DESIGN OPTIMIZATION (RBDO) OF MICROCHANNEL COOLING SYSTEMS

The deterministic provides useful hints in a design process. However, the design variable variances may destroy the harmony. And the design uncertainties can be controlled within acceptable range but can be barely eliminated. Thus, it is crucial to obtain optimal solutions under reliability frames.

4.1 UNCERTAINTIES IN MICROCHANNEL SYSTEM

The design uncertainties are not well studied in microchannel systems. Therefore, a few assumptions regarding the design uncertainties are made in advance. Those are: (1) Each design variable follows a Gaussian distribution; (2) The default standard derivation equals 5% or 10% of the mean value. From the 3-sigma rule, about 68%, 95%, and 99.7% of the values drawn from the distribution are within one sigma, two sigma, and three sigma away from the mean. These aspects are shown in Figure 32.

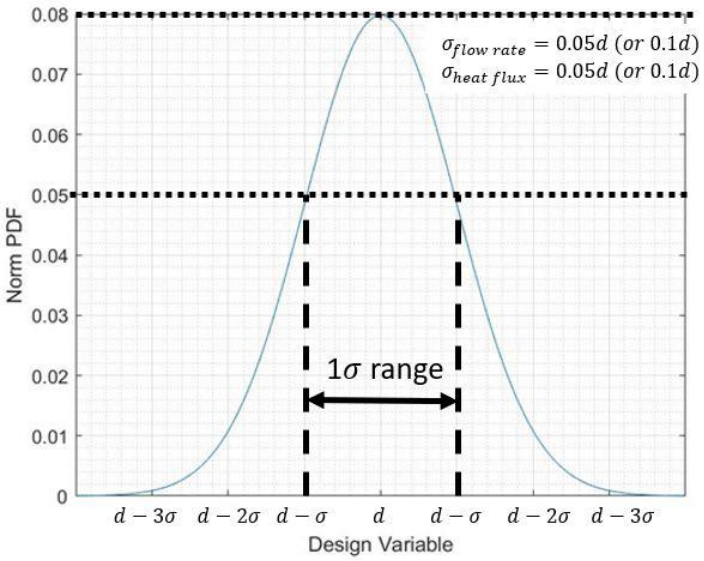

Figure 32 The design variable distributions for the flow rate and heat flux.

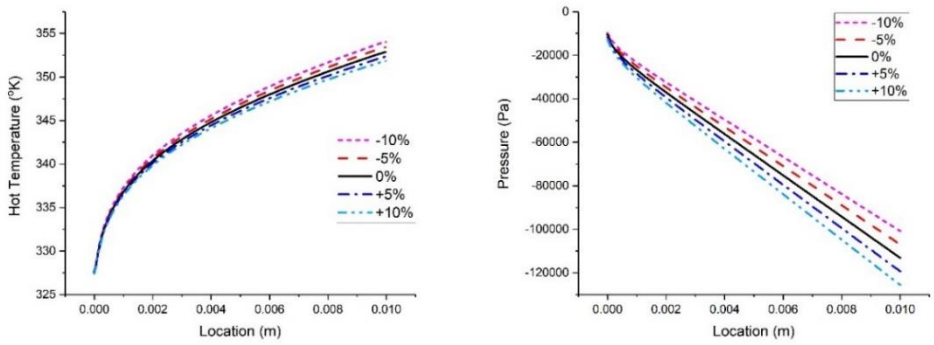

Figure 33 The effects of the flow rate uncertainty on the hot-spot temperature and pressure drop.

The flow rate fluctuates due to many reasons such as an unstable pumping pressure. The flow rate variation effects are shown in Figure 33. Another cause of flow rate uncertainty is the flow non-uniformity among the channels. In practice, the flow rate could be much higher for channels in the middle regions compared to the channels on the sides of the cooling module. In the current study, we assume the total flow rate is uniformly distributed over all the channels. The flow rate uncertainty from this cause is not covered in this study.

Heat flux uncertainties arise from factors like supply voltage, and environment fluctuations. The heat flux fluctuation effects are shown in Figure 34. The heat flux uncertainty does not affect the pressure drop, but it primarily affects the hot-spot temperature by more than 5℃.

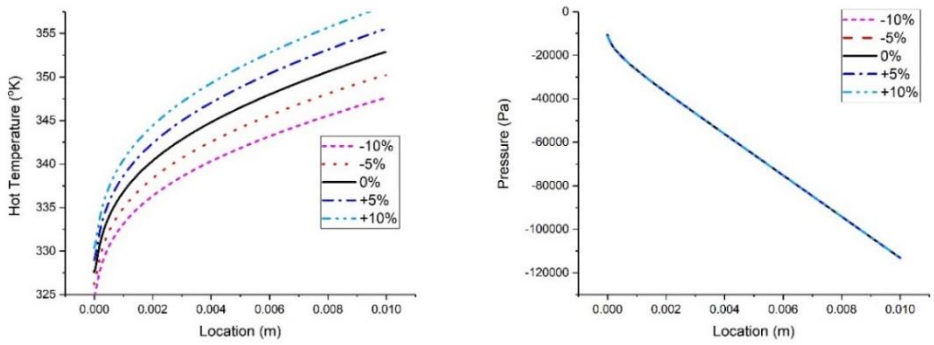

Figure 34 The effects of the heat flux uncertainty on the hot-spot temperature and pressure drop.

4.2 REVIEW OF METHODOLOGY FOR RELIABILITY OPTIMIZATION UNDER UNCERTAINTY

In this session, the common reliability optimization methods are discussed. The Performance Measure Approach (PMA) is chosen as the main reliability optimization method in this study.

4.2.1 Reliability index approach (RIA) and performance measure approach (PMA)

The main difference between the deterministic and reliability optimizations is the design constraint [20]. In reliability approaches, the design constraint is expressed as a failure probability limitation. The common form is $P(G_i(x) < 0) \leq P_{f,i}$, where G_i is the ith constraint function, and $P_{f,i}$ is the ith constraint failure limitation.

There are two ways to rewrite the probabilistic constraint, both require the help of the reliability index as $\beta_t = -\Phi^{-1}(P_f)$. Below are the equations for the two methods.

$$\beta_s = -\Phi^{-1}(F_G(0)) \geq \beta_t \tag{18}$$

$$g^* = {F_G}^{-1}(\Phi(-\beta_t)) \geq 0 \tag{19}$$

The first listed equation represents the Reliability Index Approach (RIA) [56], and the second one is the Performance Measure Approach (PMA) [20].

A linear example is used to test the robustness of the two methods. The optimization formulation is shown below.

$$\begin{aligned} Min_d \quad & d_1 + d_2 \\ s.t. \quad & P_i[g_i(X) > 0] \le P_{f,i} \\ & 0.1 \le d_j \le 10, i = 1,2 \end{aligned} \tag{20}$$

Where,

$$\begin{aligned} g_1(X) &= -X_1 - 2X_2 + 10 \\ g_2(X) &= -2X_1 - X_2 + 10 \end{aligned} \tag{21}$$

The allowable failure probabilities are 2% and 3%, respectively. The standard derivation of both design variables is $1/\sqrt{3}$.

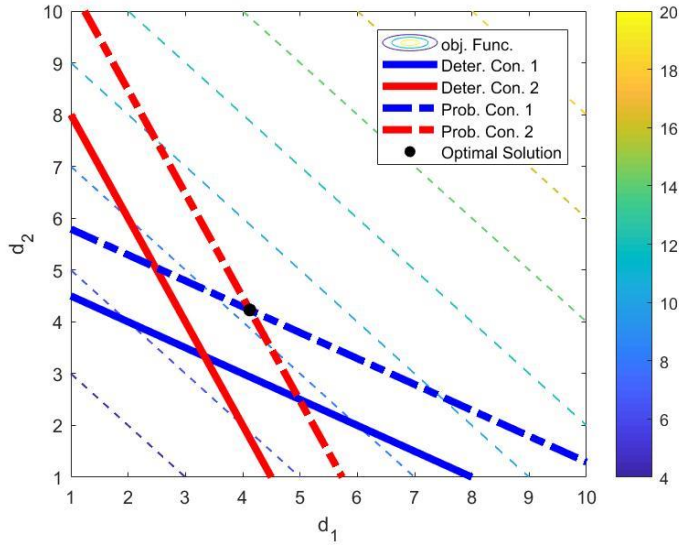

Figure 35 Linear example optimal solution.

The linear example optimization can be graphically demonstrated in above figure. However, the two methods behave differently with different initial guesses.

Table 5. RBDO using RIA and PMA with initial solution of d0 = [5, 5].

RBDO	Cost	d1	d2	Convergence
RIA	10	5	5	No
PMA	8.353	4.1230	4.2300	Yes

Table 6 RBDO using RIA and PMA with initial solution of d0 = [3.5, 3.5].

RBDO	Cost	d1	d2	Convergence
RIA	8.9506	4.3251	4.6255	No
PMA	8.353	4.1230	4.2300	Yes

Table 7 RBDO using RIA and PMA with initial solution of d0 = [4, 4].

RBDO	Cost	d1	d2	Convergence
RIA	8.3532	4.1234	4.2298	Yes
PMA	8.353	4.1230	4.2300	Yes

From the above table, RIA method is very sensitive to initial guesses. For four selected initial guess pairs (2, 2), (3.5, 3.5), (5, 5) and (4, 4), RIA only converged for initial guess (4, 4). But PMA can provide converged results regardless of the initial guesses. Based on this reason, we would use PMA as our primary method in this study.

4.2.2 Benchmark examples

The PMA code is validated by running a nonlinear benchmark example. This is a well-defined reliability-based design optimization problem [57]. In this problem, there are three nonlinear probabilistic constraints. Also, the optimal solution is to be determined. The mathematical formulation is listed below. The objective is to minimize the summation of d_1 and d_2. The design constraints are $g_1(X)$, $g_2(X)$, and $g_3(X)$.

$$\begin{aligned} Min_d \quad & d_1 + d_2 \\ s.t. \quad & P_i[g_i(X) > 0] \le P_f \\ & 0.1 \le d_j \le 10, i = 1,2,3 \end{aligned} \tag{22}$$

where

$$\begin{aligned} g_1(X) &= 1 - \frac{X_1^2 X_2}{20} \\ g_2(X) &= 1 - \frac{(X_1 + X_2 - 5)^2}{30} - \frac{(X_1 - X_2 - 12)^2}{120} \\ g_3(X) &= 1 - \frac{80}{X_1^2 + 8X_2 + 5} \end{aligned} \tag{23}$$

The reliability results are shown in Figure 36. The blue, red, and purple solid lines represent the deterministic form of the three design constraints respectively. The dash lines are the probability design constraints that guide the reliability optimization. And the computed optimal solution $[d_1, d_2] = [3.44, 3.29]$ matches with the benchmark results [57]. The objective and constraint functions are polynomial functions like this nonlinear example. For this reason, this benchmark nonlinear example can serve as validation of the reliability method as well.

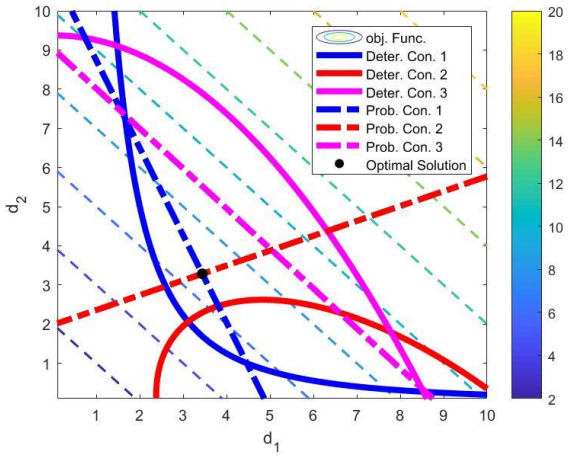

Figure 36 Application of PMA on a nonlinear benchmark problem.

4.2.3 PMA for microchannel cooling systems

In Performance measure approach, one reliability optimization formulation is divided into two deterministic sub-problems. The first sub-problem aims to find the most probable points (MPP) in the transformed standard normal space (u-space). The MPPs u_1^{k+1} and u_2^{k+1} will be employed to evaluate the target performance measure g_1^* and g_2^* in the second sub-problem.

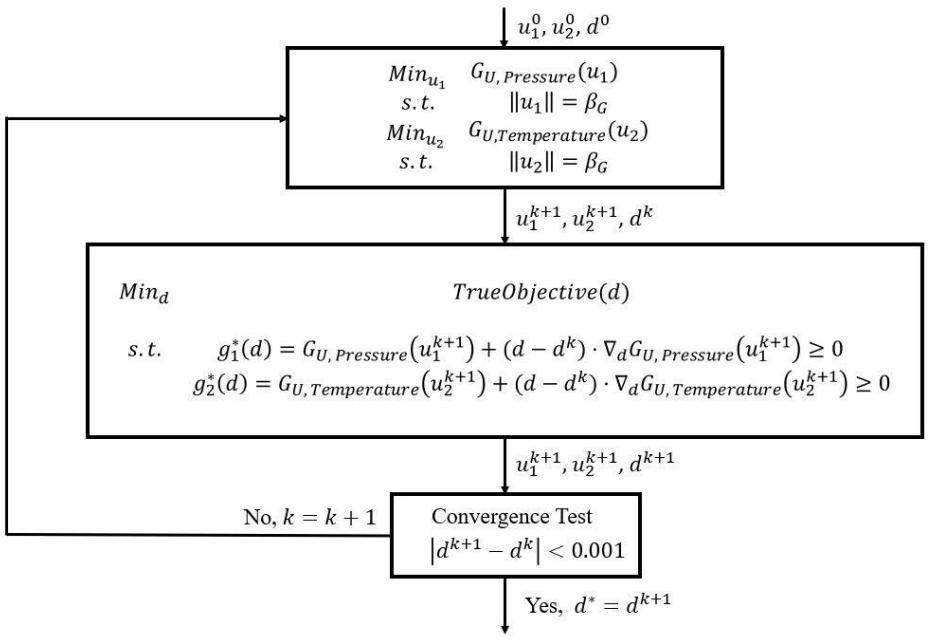

Figure 37 Flowchart representation of the PMA in microchannel cooling application.

The detailed optimization process is illustrated in Figure 37. In this figure, the system constraints are taken into consideration through the system performance functions in u-space G_U. The initial guesses of the MPPs, $u_1^0\ and\ u_2^0$, together with the optimal solution guess d^0 are provided to the MPP sub-problems. In MPP, the objective function is the transformed constraint functions in the u-space. The target reliability index β_G is used as the constraint. The prescribed failure probability P_f is closely related to the target reliability index β_G in the form of $\beta_G = -\Phi^{-1}(P_f)$. Φ is the Standard normal cumulative distribution function (CDF). In the microchannel cooling application, there are two probability constraints, one for the pressure drop and the other for the hot-spot temperature; thus, two MPP sub-problems are solved.

Using the updated MPPs and the optimal solution from the last iteration, the probability constraints are evaluated as linear deterministic constraints. Moreover, this sub-problem can be easily solved in the same method of the deterministic optimization process. The converged solution d^* is the optimal reliability solution.

4.3 SINGLE- AND MULTI- OBJECTIVE OPTIMIZATION

The three design variables to be optimized are the flow rate, the number of channels (channel width) and heat flux. The uncertainties of flow rate and heat flux are considered in the optimization. Reliability optimization were performed for two different sets. In Set (I), the flow rate and the number of channels are the two design variables. In Set (II), the flow rate and heat flux are the design variables. The reliability optimization results and some important conclusions are made based on the probability optimization outcome.

4.4 PARETO FRONT OPTIMIZATION

The probability optimization formulation for the first set is shown in the equation below. Two conflicting functions, dimensionless thermal resistance, and dimensionless pumping power are listed as the objectives. Hot-spot temperature and pressure drop served as two probability constraints. The failure probability is chosen as 0.13% based on three-sigma rule. A varying factor ω is steadily adjusted from 0 to 1 with the intervals being 0.01. In total, the reliability optimization formulation is repeated 100 times. Thoese one hundred optimal solutions lead to the Pareto frontier. Compared to the Pareto frontier, there is no other solution that shows smaller thermal resistance and pumping power at the same time. The Pareto frontiers are the most efficient solutions.

$$\begin{aligned} Min_{\dot{V},\, W} \quad & \omega \frac{\theta}{|\theta_{max}|} + (1-\omega) \frac{Power}{|Power_{max}|} \\ s.t. \quad & P_1[Pressure \geq 3\ atm] \leq 0.13\% \\ & P_2[Temperature \geq 90℃] \leq 0.13\% \\ & 5 \leq \dot{V} \leq 100\ m\,l/m\,in \\ & 20 \leq W \leq 100\ um \\ & 0 \leq \omega \leq 1 \end{aligned} \tag{24}$$

The optimization results for Set (I) in the design variable space are shown in Figure 38. The blue solid line is the deterministic pressure constraint, and the red solid line is the deterministic hot-spot temperature constraint. On the upper side of the pressure constraint, the design has a low flow rate and high channel width. The pressure-drop does not exceed the pressure-drop constraint. On the right-side of the temperature constraint, the design has a low channel width and a high flow rate. The hot-spot temperature does not exceed the hot-spot temperature constraint. The dotted points represent the Pareto frontier.

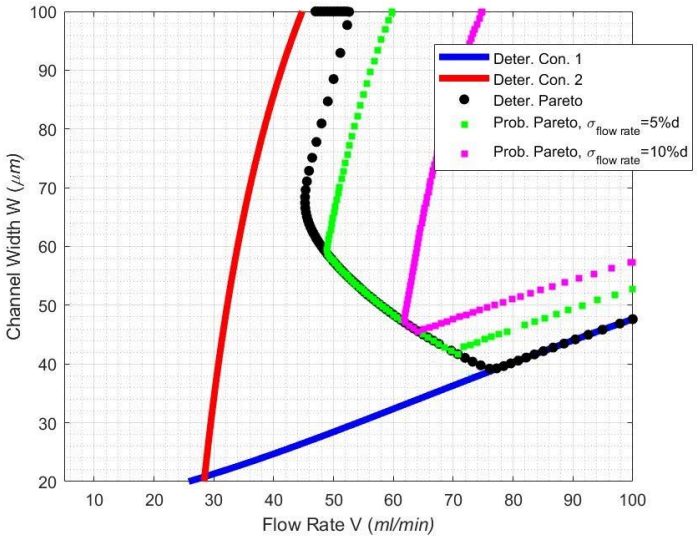

Figure 38 Deterministic and probabilistic Pareto frontiers for Set (I) in the design variable plane.

In above figure, three series of Pareto frontiers are compared. The black circle dots represent the deterministic Pareto frontiers. The green and purple square dots are the probabilistic Pareto frontiers with uncertainty levels of 5% and 10%. The red and blue solid lines are the deterministic hot-spot temperature and pressure drop constraints. The Pareto frontier with uncertainty lies farther away from the design constraint. Such shift prevents the system failure with a 5% design variable fluctuation. When the uncertainty level is increased from 5% to 10%, the Pareto frontier moves even farther away from the design constraint.

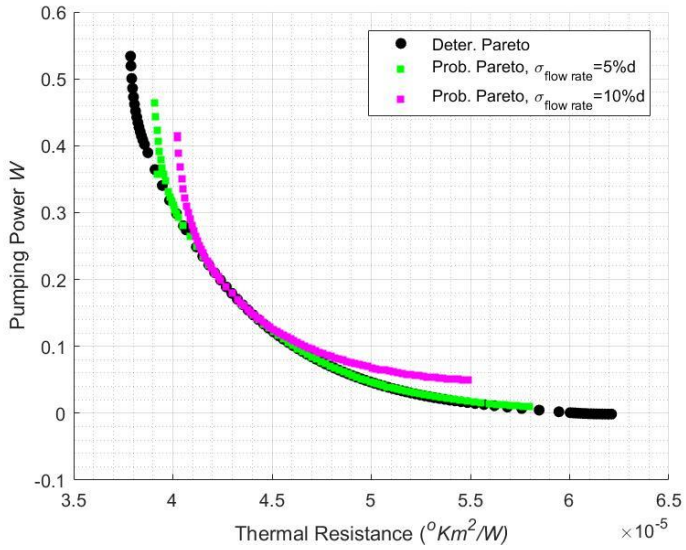

Figure 39 Deterministic and probabilistic Pareto frontiers for Set (I) in the objective plane.

Another perspective is to project the Pareto frontiers in the objective plane. The figure above shows the required pumping power and the corresponding thermal resistance for the Pareto frontiers. Compared to deterministic optimization results, higher pumping power is needed under design uncertainties. Thus, this figure can be used by a designer or operator to use trade-off between pumping power and thermal resistance to choose the desired operating point. Higher pumping power is needed for lower thermal resistance, as expected, and lower pumping power for higher thermal resistance. Depending on the available pumps and desired operation of the system, one could choose the most appropriate operating conditions.

Set (II): Flow rate and heat flux

In the second optimization set, the flow rate and heat flux are the design variables. The equation below shows the optimization formulation.

$$
\begin{aligned}
Min_{\dot{V},\ q''} \quad & \omega \frac{\theta}{|\theta_{max}|} + (1-\omega)\frac{Power}{|Power_{max}|} \\
s.t. \quad & P_1[Pressure \geq 3\ atm] \leq 0.13\% \\
& P_2[Temperature \geq 90℃] \leq 0.13\% \\
& 5 \leq \dot{V} \leq 250\ m\,l/m\,in \\
& 20 \leq q'' \leq 80\ W/cm^2 \\
& 0 \leq \omega \leq 1
\end{aligned}
\tag{25}
$$

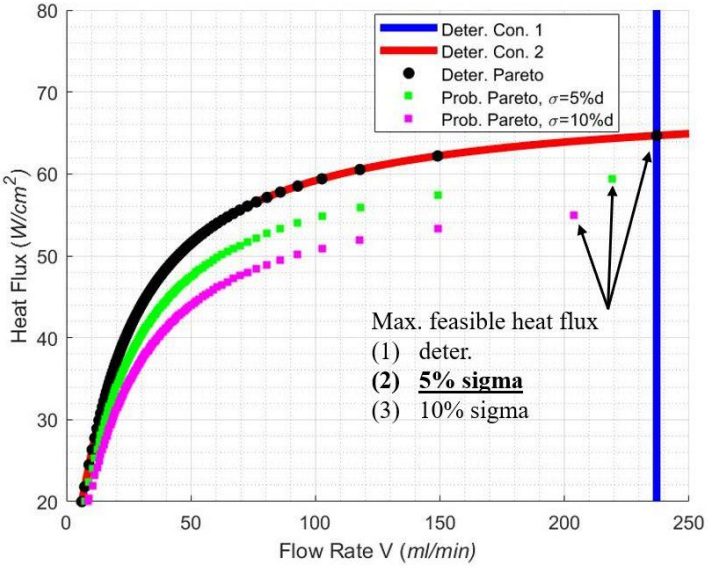

Figure 40 Optimal solution for minimizing the thermal resistance.

The Pareto frontiers are shown in Figure 40. With the existence of pressure drop and hot-spot temperature constraints, there is a maximum feasible heat flux, which is the intersection point of the two constraints. Moreover, this maximum feasible heat flux shifts to lower values under design uncertainties. Compared to the deterministic case of 64.6 W/cm^2, the maximum feasible heat flux reduces to 59.4 W/cm^2 and 55.1 W/cm^2 for uncertainty levels of 5% sigma and 10% sigma, respectively. The maximum feasible heat flux is the maximum heat flux value that the system can sustain without any danger of

system failure. In this study, the considered system failure factors are hot-spot temperature and pressure drop constraints.

4.5 MAXIMUM FEASIBLE HEAT FLUX

The default pressure-drop constraint value is taken as 3 atm, and the default hot-spot temperature constraint value is taken as 90 ℃. Under these constraints and default design conditions, the obtained maximum feasible heat flux is 59.4 W/cm^2. The design constraint effect on the maximum feasible heat flux is shown in Figure 41. In Figure 41 (a), the temperature constraint is set at constant values of 80, 90, and 100 ℃, and the pressure constraint is changed from 0.1 atm to 10 atm. In Figure 41 (b), the pressure constraint is set at constant values, and the temperature constraint is changed from 60 ℃ to 120 ℃. The same approach is repeated multiple times to collect the maximum feasible heat flux responses.

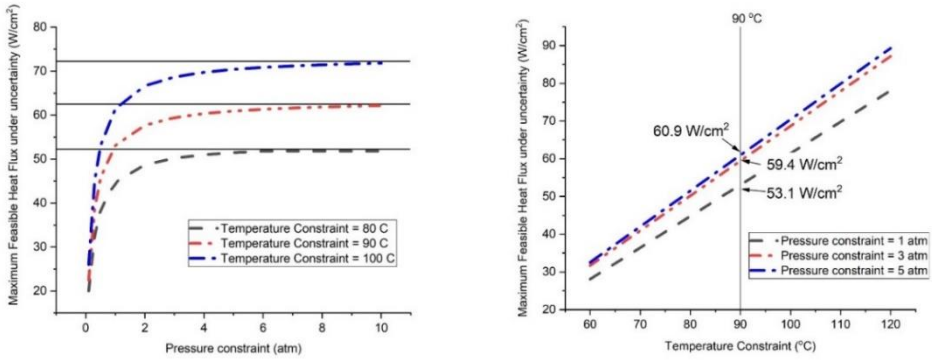

(a) (b)

Figure 41 Effects of the design constraints on the maximum feasible heat flux.

The maximum feasible heat flux increases almost linearly at smaller pressure drop ranges and reaches its plateau value at larger pressures. Any further pressure constraint increase, larger than ~ 6 atm, has almost no influence on the maximum feasible heat flux value.

On the other hand, the temperature constraint has a linear relation with the maximum feasible heat flux regardless of the pressure constraint.

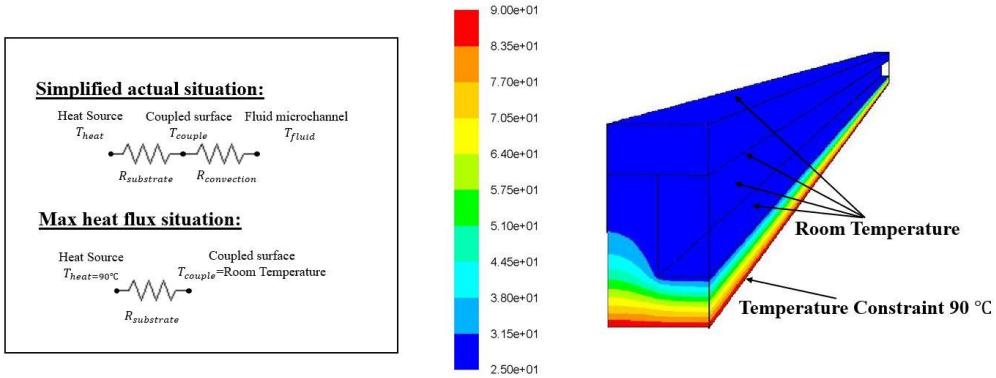

Figure 42 Explanation of the effects of the design constraints on the maximum feasible heat flux.

The Fourier's law of heat conduction can explain Figure 42. With an extremely high pressure drop constraint, the substrate part in direct contact with the fluid has about the same temperature of the fluid. Assume the entire substrate bottom reaches the hot-spot temperature, the heat conduction circuit is reduced to the maximum heat flux situation, as shown in Figure 42. According to Fourier's law, the heat conduction relation can be simplified written as the equation below:

$$q''_{max} = \frac{T_{hot-spot} - T_{fluid}}{R_{substrate}} \propto \frac{(T_{hot-spot} - T_{fluid})k}{L} \ (W/m^2) \tag{26}$$

Therefore, the maximum feasible heat plateau value exists and can be roughly estimated, and this plateau value has a linear relation to the hot-spot temperature constraint as is exhibited in Figure 41 (b).

This maximum feasible heat flux is calculated based on the single-phase liquid cooling. However, this feasible heat flux plateau value is not only applicable to the single-phase liquid

cooling but also useful for multi-phase cooling systems. To achieve higher feasible heat flux values, we recommend to either seek higher thermal conductivity substrate materials or fabricate thinner substrate bases. Both solutions require better fabrication techniques.

4.6 OPTIMAL CHANNEL CONFIGURATION

In session 3.3, the concept and physical meaning of maximum feasible heat flux are proposed. This value is obtained with fixed specific channel geometries, such as the number of channels (channel width). By changing the channel geometry, differing maximum feasible heat flux values are collected.

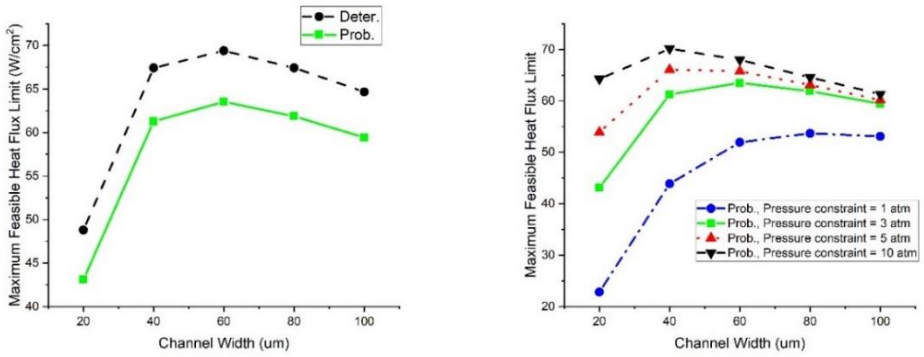

(a) (b)

Figure 43 (a) Optimal channel configuration with and without design uncertainties; (b) Optimal channel configuration under different pressure constraints.

In Figure 43 (a), the maximum feasible heat flux values under deterministic (black circle) and reliability (green square) conditions are shown. The design constraints are set as default values of 3 atm for pressure and 90 ℃ for temperature. As expected, the design under uncertainty can only sustain lower heat flux conditions compared to the deterministic design. The optimal geometry remains the same for deterministic and probability cases.

In Figure 43 (b), the maximum feasible heat flux with different pressure constraints are displayed. The hot-spot temperature constraint remains at 90 ℃. With higher pressure constraint, a higher maximum feasible heat flux can be achieved, and the optimal system geometry gradually moves to the direction of smaller channel width region. The detailed maximum feasible heat flux and its associated optimal channel configurations are shown in Table 8.

Table 8 Maximum feasible heat flux and associated system configuration.

Pressure Constraint (atm)	Max heat flux (W/cm^2)	The number of channels	Channel Width (μm)
1	53.69	62	80
3	63.52	83	60
5	66.07	125	40
10	70.16	125	40

5 OPTIMIZATION OF OTHER APPLICATIONS

The optimization method developed in this study can not only be applied to microchannel cooling system but also to any general thermo-fluid systems. Optimization of the SLM gas flow system, and the CVD system have been carried out to illustrate this point.

5.1 SELECTIVE LASER MELTING (SLM) GAS CHAMBER

This study developed a comprehensive fluid-particle interaction CFD model to simulate the gas flow effect on spatter distribution. The spatter motion trajectory is studied to better understand the particle dynamics inside the gas flow chamber. Several influential process and design parameters of the gas flow system, such as flow rate, inlet height and width, as well as material density, have been investigated to enhance the removability of the process emissions.

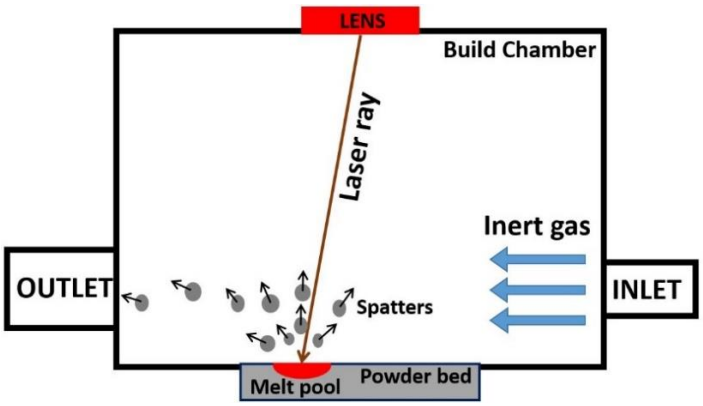

Figure 44. Graphic description of problem.

5.1.1 Numerical methods

In this study, the objective is to maximize the removal efficiency of process emissions during the SLM process. Therefore, the design of the gas flow system, including

gas inlet width, inlet height, volume flow rate, and processing materials, will be thoroughly investigated. A generic baseline SLM build chamber design (Renishaw AM250) is shown in Figure 45 (a). A CFD simulation of gas-spatter interaction has been performed to investigate the effect of gas flow on spatter distribution inside the SLM build chamber. The build chamber fluid flow is assumed to be steady, incompressible and turbulent flow; therefore, standard Navier-Stokes equations and k-ε turbulent model are used to describe the fluid characteristics.

A Discrete Phase Method (DPM) model was developed to study the spatter distribution within the SLM chamber. Spatters are generated by DPM method and fully coupled with the gas phase. To efficiently model the gas-spatter interaction inside the chamber, several assumptions have been made:

(1) Instead of generating the spatters from the melt pool level, the spatter source are modeled as five lines evenly distributed on the powder bed to cover the entire build area, as shown in Figure 45 (a).

(2) The spatter particles are ejected with three different ejection angles to the horizontal substrate: 60°, 90°, and 120°.

(3) All the ejection sources have Gaussian distributed particles ranging from diameter 20 μm to 80 μm with an ejecting speed of 3 m/s.

Different boundary conditions have been applied to different domains of the model. To calculate the spatter-chamber wall surface contact, “Wall” boundary condition with DPM settings are used. The DPM particles will be rebounded off from the “reflect” wall boundaries with a modified momentum. The trajectory calculations are terminated and recorded as “trapped” if the particles fall on “trap” wall boundaries. In this simulation, only

the powder bed surfaces, including the five spatter source lines, are listed as DPM "trap" boundary conditions. Other chamber wall surfaces are marked as "reflect" boundaries. The inert gas firstly enters the inlet rail with given flow rate, then flows into the main build chamber through a row of cylindrical nozzles with 12 mm in diameter. The gas and spatter flow out of the domain through outlet. Therefore, the gas inlet is set to be "mass flow rate" while "outflow" boundary condition is applied for the outlet. The inert gas used in the simulation is argon with a viscosity of 2.1252×10^{-5} kg/m-s and a density of 1.6228 kg/m^3. The mass flow rate is set as 0.00677 kg/s (250 L/min). Figure 45 (b) shows the model mesh information, the entire domain has ~1.5 million elements. The spatter material is SS316L with a density of 7950 kg/m^3. For all simulated cases in this study, there may be small variations in the total amount of element which is caused by the slight change of gas chamber geometry. To solve the coupled fluid-particle momentum and pressure equations, the SIMPLE (Semi-Implicit Method for Pressure Linked Equations) solution method was used.

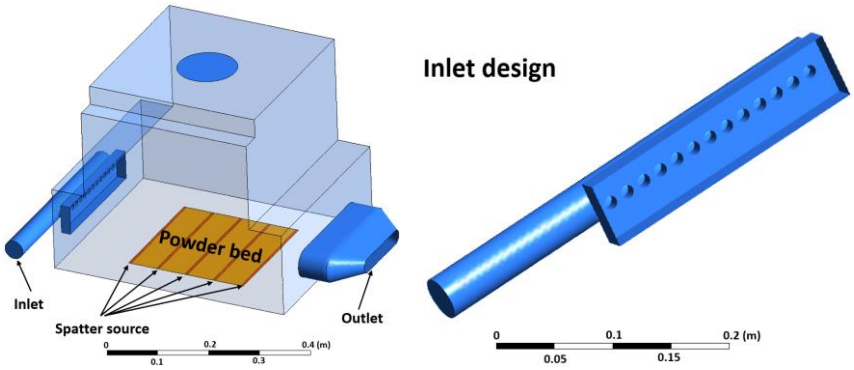

(a) Geometry of gas chamber

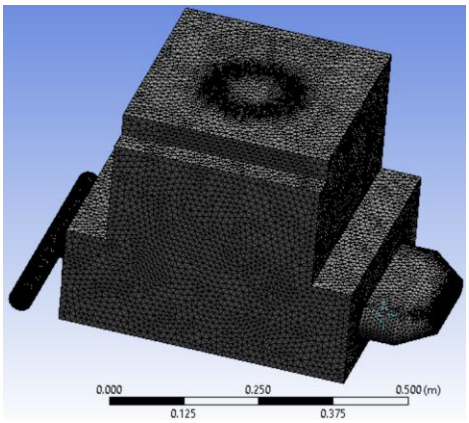

(b) Mesh used for computational domain

Figure 45. Model geometry and mesh information.

5.1.2 Overview of all design variables

In this part, one baseline design simulation is used to show the gas flow variations and particle behaviors. Afterwards, three different design parameters, inlet width, inlet height and flow rate, are adjusted to show their influence on the system and spatter removal. Finally, different spatter material, namely, AlSi10Mg, Ti64 and SS316L, have been simulated to study the particle density effect. To quantify emission removal performance, a “clear rate” is used to describe the spatter removal efficiency. The clear rate is defined as the ratio of the number of spatter particles removed out of the build region (powder bed) to the total number of spatters.

Figure 46 shows the simulation results for gas-spatter interaction in the baseline design chamber. The spatters firstly ejected to the gas chamber from the build region, then the incoming gas flow blew the particles toward the outlet. However, not all spatters can be removed from the build chamber, they may re-deposited to the chamber substrate due to gravity.

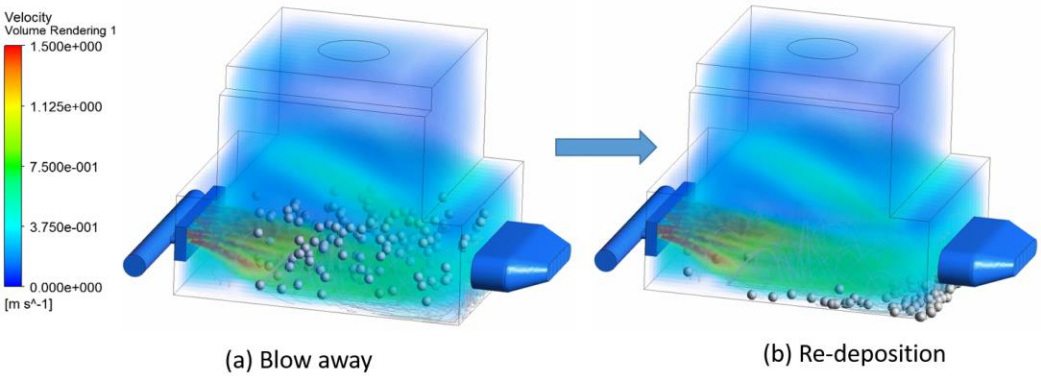

Figure 46. Typical simulation results.

Two perspectives of the velocity contours inside the system are discussed below. Figure 47 (a) is a side view of the chamber gas flow velocity contours located in the middle of the chamber. It is seen that high gas velocity streams come out of the inlet nozzles and flow down toward the substrate. The spatter trajectories are affected by the gas flow and spatters move toward the outlet. It is seen that the spatter generated in the region closest to the outlet are mostly removed. Figure 47 (b) is an isometric view of the gas flow velocity contours on the center-plane (center of inlet nozzle), where a high velocity concentration region is observed around the inlet region with a near triangular shape. The spatter distribution map shows that the substrate region close to inlet has little spatter concentration while the region close to outlet has high spatter concentration. The spatter re-deposition map generally follows the velocity contour: high velocity region has little re-deposition phenomenon. With the decrease of the inlet gas flow velocity, the spatters fall down to substrate region that is away from the inlet region, as shown in Figure 47 (b). The overall clear rate of the baseline design is 60.4%. With inert gas flow, more than half of the spatters are removed out of the built area. However, there is still around 40% spatters redeposited

on the powder bed region. And those redeposited spatters have a higher concentration on the part that is closer to the outlet.

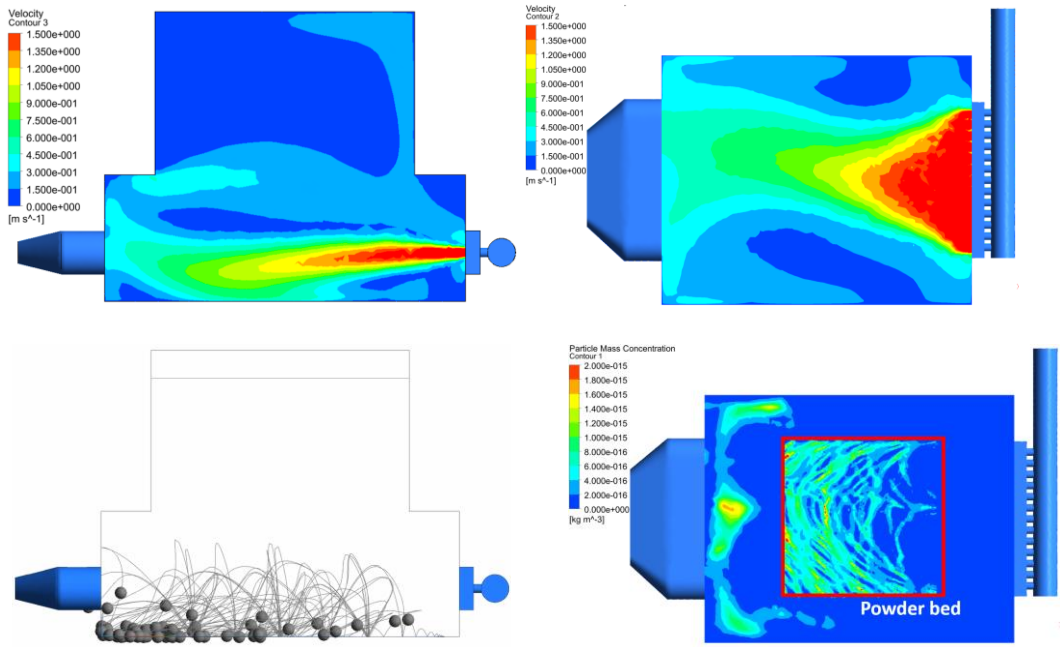

(a) Side view (b) Center-plane view

Figure 47. Velocity contours and spatter distribution of the baseline chamber design.

5.1.3 Inlet flow rate effect

The movement of the spatter is largely decided by gas flow and particle condition. Therefore, a strong inlet gas flow may help to improve spatter clear rate. Three different inlet flow rates, 0 L/min, 250 L/min and 500 L/min, were tested to investigate flow rate effect on spatter distribution. A flow rate of 0 L/min means no gas flow is applied. The spatters simply eject outward then fall back under the gravity force. The drag force imposed on the particles is little due to the negligible gas flow rate. With the increase of flow rates, the gas flow starts to affect the particle motion and the spatter trajectory changes

significantly, e.g., the spatter motion trajectories are hard to reach outlet for 0 L/min case while majority of the spatters go toward the outlet for 500 L/min case, as shown in Figure 48. The clear rate for the three cases are: 0%, 60.4%, 81.1% for 0 L/min, 250 L/min, and 500 L/min respectively. Therefore, higher flow rate is helpful for spatter removal.

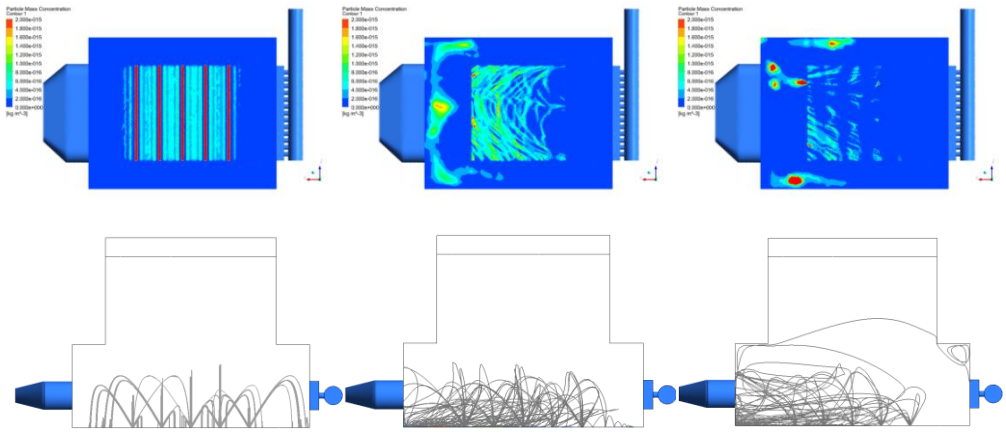

(a) 0 L/min (b) 250 L/min (c) 500 L/min

Figure 48. Spatter re-deposition maps and trajectories with different flow rates.

5.1.4 Inlet width effect

The inlet width has been varied proportionally to study the inlet width effect, all other parameters are kept unchanged as the baseline case, e.g., a flow rate of 250 L/min is used. The nozzle to nozzle distance has been adjusted accordingly. The effects of three inlet widths of 225 mm, 250 mm and 275 mm were compared, as shown in Figure 49. The flow field differences between different inlet width cases are subtle. In all cases, the flow velocity is stronger in the middle of the chamber, but this effect is particularly noticeable for a smaller inlet width. Larger inlet widths such as 275 mm, results in a lower gas flow velocity above the build area which diminishes the particle removal efficiency. An inlet width with same or similar width as the build region (powder bed) width of 250 mm is

shown to be most effective, as the highest particle clear rate of 60.4% with the inlet width of 250 mm, compared to the rate of 60.0% for a narrower width of 225 mm and 59.3% for a wider width of 275 mm.

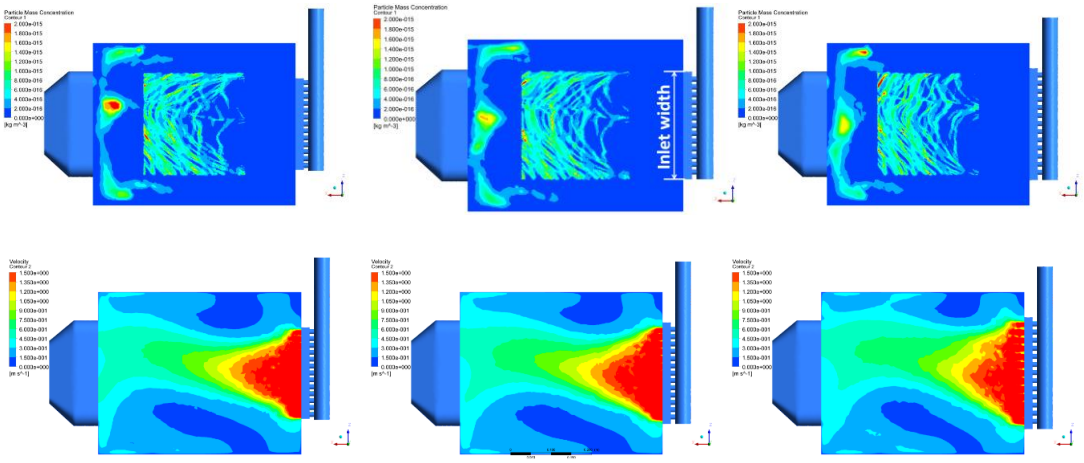

(a) Width = 225 mm (b) Width = 250 mm (c) Width = 275 mm

Figure 49. Spatter re-deposition maps and velocity contours with different inlet widths.

5.1.5 Inlet height effect

The inlet height effect on spatter re-distribution is also investigated. Inlet height is defined as the distance from the center plane of inlet nozzles to the substrate plane. Three designs with different inlet heights: 50 mm, 67.5 mm and 85 mm are compared in this section while all other parameters are the same as the baseline case. Figure 50 shows the re-deposition maps and velocity contours at center vertical plane. It is found that the case with inlet height equal to 67.5 mm (Figure 50 (b)) removes the most particle emissions (60.4% clear rate). Lower inlet height design (Figure 50 (a)) has a clear rate of 59.8%, and higher inlet height design (Figure 50 (c)) has a clear rate of 57.7%. It demonstrates that a

moderate inlet height is preferred to remove the most particles. It is observed that the high gas velocity region moves up and down together along with the inlet height modifications. The spatters have pre-defined initial ejection velocities, and it falls after reaching a peak height due to gravity. Therefore, spatters may penetrate the high velocity region with a low inlet height design. On the other hand, the high gas velocity region may be too high to exhibit influence on the spatter particles for a high inlet height design case.

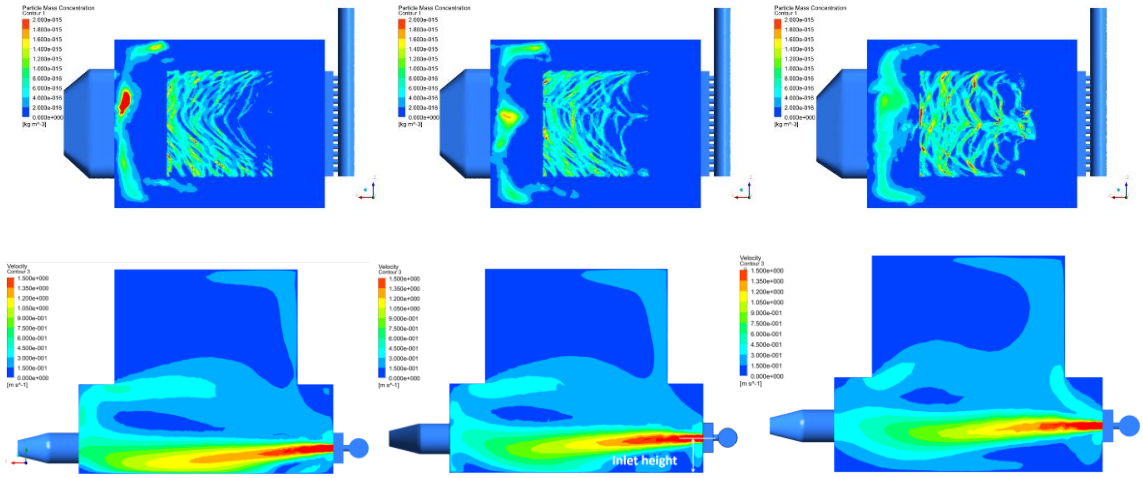

(a) Height = 50 mm (b) Height = 67.5 mm (c) Height = 85 mm

Figure 50. Spatter re-deposition maps and velocity contours with different inlet heights.

5.1.6 Spatter material property effect

To examine the effects of the spatter material property, three materials are chosen and compared using the baseline case. The three common SLM materials are AlSi10Mg, Ti64, and SS316L. The corresponding densities are about 2700 kg/m^3, 4400 kg/m^3 and 7950 kg/m^3. Even though the interactions between the particle and gas fluid are considered

in the simulations, the influence of the particle on the gas fluid field is minor such that the velocity fields remain almost the same for these three cases. Figure 51 shows the spatter particle trajectories of the three materials. It is shown that the spatter material is also a significant factor for the system design. The particle trajectory with lighter material shows higher flow pattern similarity to the gas flow velocity field. This can be explained that the ratio between the flow drag force and the gravity will be larger for a lower density spatter material. Therefore, the individual particle motion is dominated by fluid drag force. The clear rate is higher for lighter materials, e.g., 69.4% for AlSi10Mg, 68.3% for Ti64 and 60.4% for SS316L.

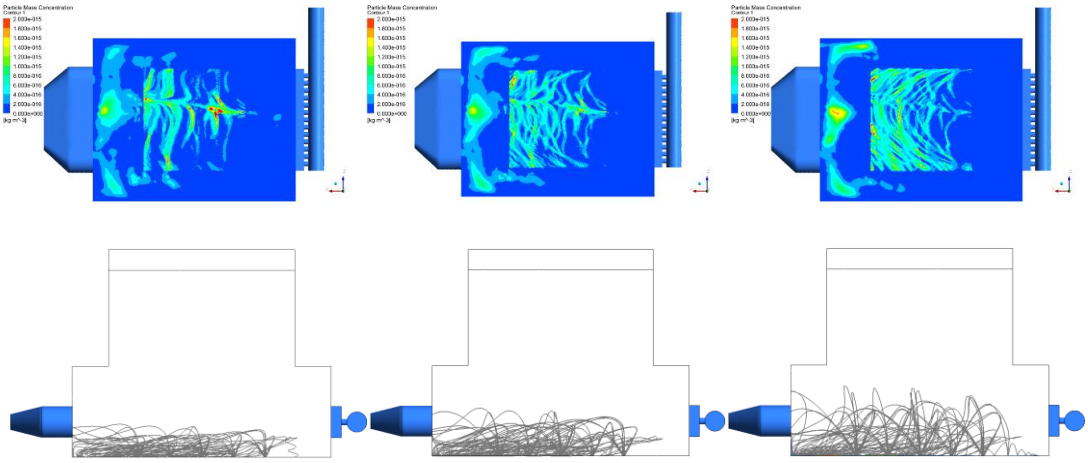

(a) AlSi10Mg (b) Ti64 (c) SS316.

Figure 51. Spatter re-deposition maps and trajectories with different processing materials.

5.1.7 Optimization of SLM gas chamber

The design variables or operating conditions of inlet pattern, volume flow rate, inlet height, inlet width, and build materials have been weighted. A summary of the important findings is in the table.

Table 9. SLM gas flow system design and optimization considerations.

Design variable	Objectives	Optimal value
Inlet pattern	Provide uniform gas flow	Pattern 2
Volume flow rate	Large enough to remove the spatter generation but not to move the powder in the powder bed	250 L/min
Inlet height	Moderate height at which the spatter particle acceleration is small.	60 mm
	Lower height has minor effects to modify the upward motion of spatter. With a high inlet height design the particles cannot travel high enough to the main gas flow layer.	
Inlet width	Same or similar width with the build area width.	300 mm
	With a smaller inlet width, the flow is non-uniform over the build plate. A larger inlet width results in a lower particle removal capability.	
Secondary inlet	Help in removing the particles and prevention of contamination of the lens	N/A

In addition to the above design and optimization table, one sample optimization formulation is given as the equation below.

$$\begin{aligned} Min_x \quad & \omega * ClearRate + (1-\omega) * EscapeRate \\ s.t. \quad & u_{max,1mm} \leq u_{limit} \\ & 0 \leq \omega \leq 1 \end{aligned} \tag{27}$$

In above equation, $u_{max,1mm}$ is the maximum velocity of the 1mm above substrate plane. This constraint is listed to prevent the risk of additional blown-up particles. Under this formulation, we can obtain the Pareto Frontiers of the SLM gas flow system. Due to the complexity of the SLM simulation and our limited computational resources, the Pareto frontiers are not calculated in this study.

The major findings can be summarized as follows:

(1) The flow rate has considerable effect on the spatter particle removing process. It is observed that a higher flow rate can significantly affect the spatter moving trajectory toward the outlet, which can contribute to obtain a higher clear rate, e.g., a clear rate of 81.1% for a flow rate 500 L/min while it is 60.4% for a flow rate of 250 L/min.

(2) Three inlet widths were compared using the developed model. It is found that the inlet width has minor effects on the clear rate. An inlet width that is similar to the width of the build area (powder bed region) shows best performance for clear rate.

(3) The effect of inlet height has been investigated. Spatters may penetrate the high velocity region (low inlet height design), or the high gas velocity region may be too high to blow away spatters (high inlet height design). A moderate height is preferable for spatter removals.

(4) The spatter material have a noticeable effect on particle motion trajectory and clear rate. A higher similarity to the gas flow velocity stream field is shown for the

trajectory of lighter spatters. It is because the spatter motion is dominated by fluid drag force for low density spatter. Therefore, higher clear rate is expected for lighter spatters, e.g., clear rate is 69.4% for AlSi10Mg while it is 60.4% for SS316L.

5.2 CVD SYSTEM

The film growth rate and uniformity are two major issues in the metal organic chemical vapor deposition (MOCVD) mass production. Our simulation has shown that they cannot be improved at the same time, so the optimization of MOCVD system is needed.

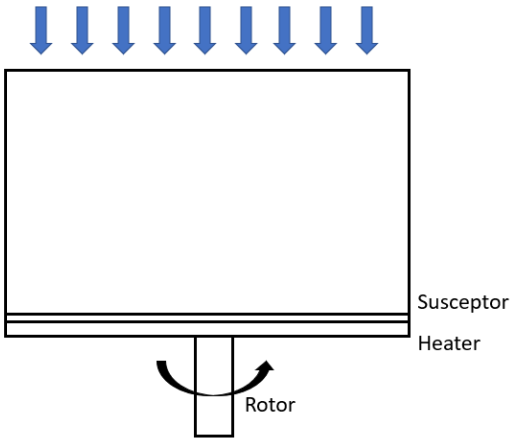

Figure 52 MOCVD system representation.

In this study, the MOCVD process is numerically simulated using CFD method [58, 59]. The conservation of mass, momentum, energy, and species are solved. The sophisticated species transport and chemical reactions in the CVD process are also computationally modelled.

5.2.1 Parametric modelling of CVD system

There are multiple ways to perform the parametric modelling of the CVD system. One is polynomial fitting, the other one is the radial basis function (RBF) fitting. The

equations used are detailed introduced in session 4.2 and will not be repeated here. Both fitting models are tested with the same data sets. The two chosen operating conditions are the TMG flow rate (slm), and the chamber Pressure (torr). A 5*5 data set is collected over the entire design domain.

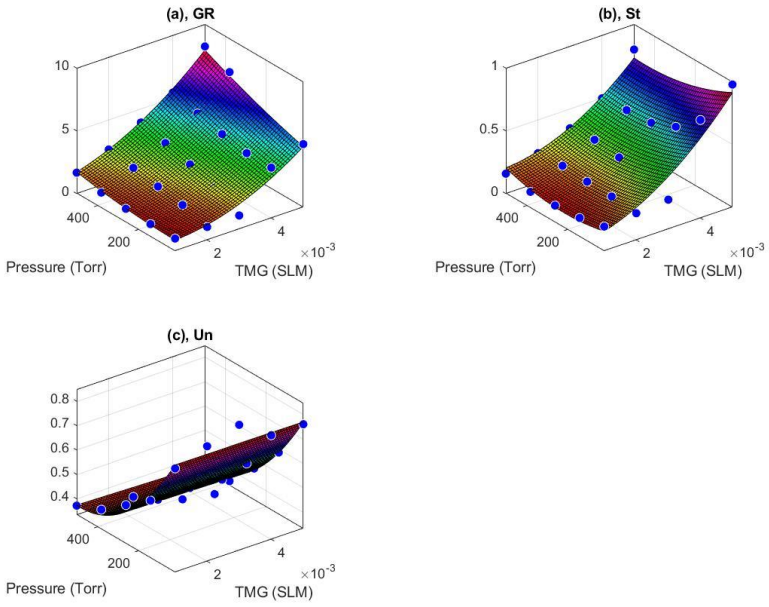

Figure 53 Polynomial parametric modelling of CVD system.

The MOCVD system has various local behavior patterns. From the figure above, the Polynomial modelling has negligible errors on multiple regions. These errors remain even if higher-order quadratic function is used. This is due to the limitations of polynomial models. With a lower degree model, the equation cannot capture the complex response variations. And the polynomial equation overfits the response with higher degree models. The disadvantages of polynomial models made it difficult for the response modelling of the CVD systems.

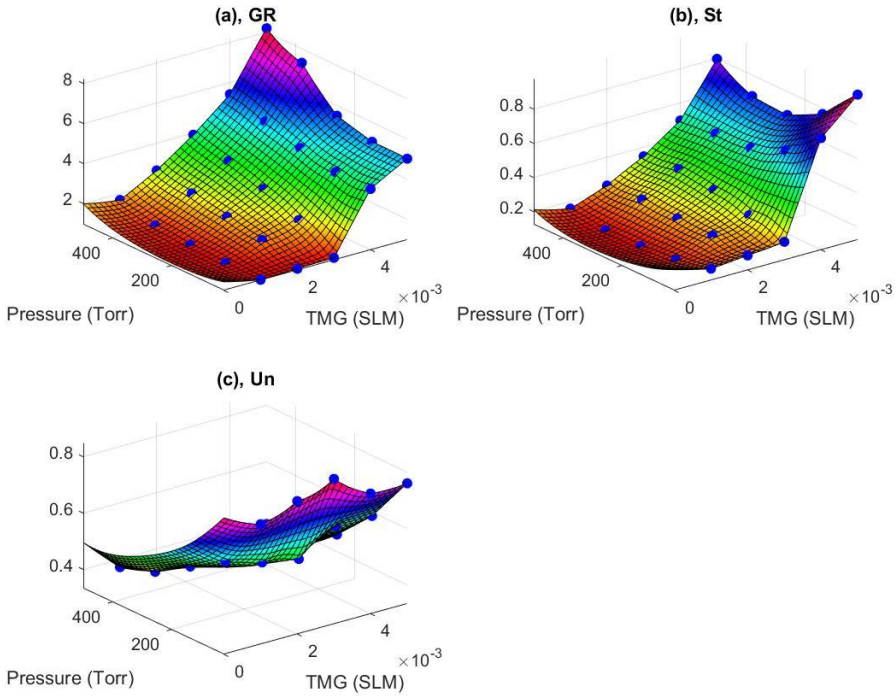

Figure 54 Radial basis function (RBF) parametric modelling of CVD system.

Compared to the polynomial model, the RBF model performs a lot better in the local response behavior. From the figure above, the RBF model always passes through the data sets points, and the resulting function captures the response in a better manner. We will use the RBF modelled results for the CVD optimization.

5.2.2 Optimization of CVD system

Two single-objective deterministic optimizations are completed. One is to minimize the film thickness standard derivation, the other one is to maximize the film growth rate. To maximize an objective function, we can simply minimize the reverse of the objective function.

$$\begin{aligned} &Min_{TMG,P} \quad Standard\ Derivation \\ &s.t. \qquad\qquad Un \leq 0.5 \end{aligned} \tag{28}$$

$$Max_{TMG,P} \quad Growth\ Rate$$
$$s.t. \qquad Un \leq 0.5 \tag{29}$$

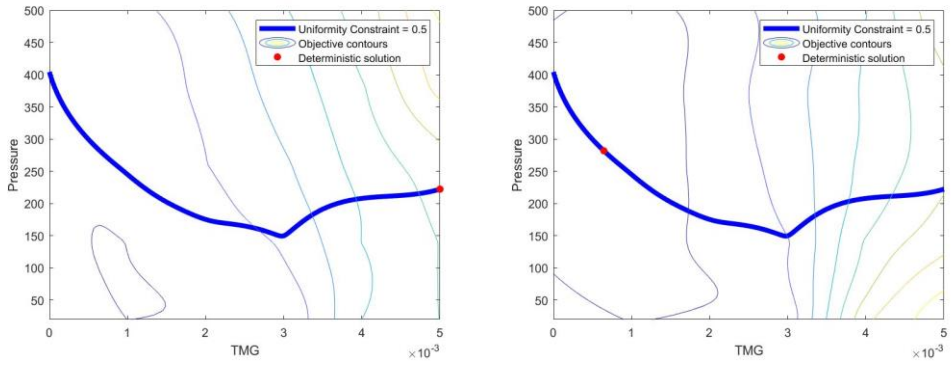

Figure 55 Single-objective deterministic optimization of the CVD system: (left) Maximization of the film Growth rate; (right) Minimization of the system Standard derivation.

Figure 55 shows the location of the two optimization solutions. It is obvious that these two objectives are not consistent, meaning that they cannot be met at the same time. If we examine the objective contours more carefully, the solution that maximize the film growth rate has a very high standard derivation. Similarly, the solution that minimize the standard derivation has a poor growth rate. This finding implies that a multi-objective formulation is necessary to provide more useful optimization solutions.

6 CONCLUSIONS AND FUTURE WORK

6.1 SUMMARY

In this study, we carried out the numerical simulation and optimizations regarding microchannel cooling system, chemical vapor deposition system, and selective laser melting gas flow system.

Numerical simulations of the microchannel system are carried out. The simulation is validated with analytical and experimental results. Based on the simulation results, response surfaces are obtained. For microchannel cooling systems, two important practical concerns exist. Hot-spot temperature may damage the device. Also, most of the hydro pumps, with dimensions comparable to the cooling area, cannot provide a pressure higher than 3 atmospheres. So, a hot-spot temperature of 90 ℃ and a pressure drop of 3 atmospheres are taken as two constraints. In the single-objective optimization, these two targets are conflicting. If we try to minimize the pumping power, the optimal solution is close to the temperature constraint boundary, while it is close to the pressure constraint boundary when reducing the thermal resistance is the only goal.

An acceptable and reliable microchannel heat removal system design requires minimization of pumping power and thermal resistance at the same time. So multi-objective optimization is carried out. Different weight factors on pumping power and thermal resistance are taken. The optimal solutions form Pareto frontiers. These are the best designs for this microchannel heat removal system without considering design uncertainty. As one tries to reduce the thermal resistance, the pumping power increases. So, a trade-off is needed for a practical and realistic system. Under given pressure and

temperature constraints, there is an optimal geometry that can remove the maximum heat flux. Variations from the optimal geometry will lower the overall performance.

The performance measure approach is used to carry out a reliability optimization for a microchannel cooling system. Design uncertainties of the flow rate and heat flux are considered. The two design constraints employed are the pressure drop constraint and the hot-spot temperature constraint.

Besides the microchannel cooling system, the numerical simulations of the SLM gas chamber and CVD system are carried out. For the SLM system, a fully coupled CFD-DPM model has been developed to investigate the gas flow effect on spatter distribution inside the SLM build chamber. In addition, the spatter generation is modeled by DPM model. The influence of different build chamber parameters, such as inlet flow rate, inlet width and height, and spatter materials, have been studied. For the CVD system, the fluid flow, heat transfer, chemical reactions, and species transport are simulated. RBF are used to generate the response surfaces for CVD system. Using the same optimization technique, we can obtain the optimal solutions of the CVD system.

Some of the important conclusions are:

(1) The performance measure approach is proven to be a useful tool in the thermal system optimization under design uncertainties.

(2) In the microchannel cooling system, compared to the deterministic designs, higher pumping power is required under design uncertainties to maintain the same thermal performance.

(3) For a microchannel cooling application, there exists a maximum feasible heat flux. With the default design constraints, this maximum feasible heat flux is obtained as

63.52 W/cm^2 under design uncertainties. The physical meaning of this value is explained. This value is dependent on factors like design uncertainties, design constraints, and geometry designs. The plateau heat flux value is mainly limited by substrate thickness and substrate materials.

(4) Under specific design constraints, there is an optimal geometry design that provides the highest thermal performance. Moreover, this optimal geometry favors smaller channel width designs as the pressure drop constraints is increased.

(5) The parametric modelling and the optimization technique can be applied to other thermo-fluid systems such as SLM gas chamber and CVD systems.

6.2 FUTURE WORK

In this study, an optimal geometry design and a maximum feasible heat flux are found. Based on the physical explanation, the maximum feasible heat flux is limited by the thermal conductivity of the substrate material and the hot-spot temperature. Section 3.4.4 further illustrates the importance of substrate materials. One interesting topic is to change the substrate material from silicon to other superior conductive materials. Examples are Silicon carbide (SiC), diamond, and copper. Under the same heat input condition, the hot-spot temperature of the microchannel systems with such better conductive substrate materials should be significantly lower compared to the silicon substrate case. And the hot-spot temperature constraint will be less severe than current cases.

Another focus for the future work is on the bio-medical applications. The thermal effects on the microchannel-based bio-medical devices are rarely studied. Blood vessels can also be categized as microchannels. And the heat transfer within blood vessel flows

needs further detailed study. Other topics related with microchannels could be: channel shape effects, fluid property study and transient behaviors.

7 BIBLIOGRAPHY

[1] Kandlikar, S., S. Garimella, D. Li, S. Colin, and M. R. King. Heat transfer and fluid flow in minichannels and microchannels. elsevier. 2005.
[2] Sobhan, C., S. Thomas, and G. Peterson. Microscale transport phenomena for bio-engineering applications: Recent advances. Journal of Advances in Nanomaterials 2. 2017.
[3] Kandlikar, S. G., and W. J. Grande. Evaluation of single phase flow in microchannels for high heat flux chip cooling—thermohydraulic performance enhancement and fabrication technology. Heat transfer engineering 25:5-16. 2004.
[4] Jaluria, Y. Microchannel Flows as Heat Sinks. In: Encyclopedia of Nanotechnology. B.Bhushan, ed. Springer Science+Business Media Dordrecht. 2015.
[5] Lee, P.-S., S. V. Garimella, and D. Liu. Investigation of heat transfer in rectangular microchannels. International Journal of Heat and Mass Transfer 48:1688-1704. 2005.
[6] Sui, Y., C. Teo, P. S. Lee, Y. Chew, and C. Shu. Fluid flow and heat transfer in wavy microchannels. International Journal of Heat and Mass Transfer 53:2760-2772. 2010.
[7] Kandlikar, S. G., S. Colin, Y. Peles, S. Garimella, R. F. Pease, J. J. Brandner, and D. B. Tuckerman. Heat transfer in microchannels—2012 status and research needs. Journal of Heat Transfer 135:091001. 2013.
[8] Yuan, W., J. Zhao, C. P. Tso, T. Wu, W. Liu, and T. Ming. Numerical simulation of the thermal hydraulic performance of a plate pin fin heat sink. Applied Thermal Engineering 48:81-88. 2012.
[9] Ghaedamini, H., P. Lee, and C. Teo. Developing forced convection in converging–diverging microchannels. International Journal of Heat and Mass Transfer 65:491-499. 2013.
[10] Xie, G., F. Zhang, B. Sundén, and W. Zhang. Constructal design and thermal analysis of microchannel heat sinks with multistage bifurcations in single-phase liquid flow. Applied thermal engineering 62:791-802. 2014.
[11] Xia, G., J. Jiang, J. Wang, Y. Zhai, and D. Ma. Effects of different geometric structures on fluid flow and heat transfer performance in microchannel heat sinks. International Journal of Heat and Mass Transfer 80:439-447. 2015.
[12] Husain, A., and K.-Y. Kim. Optimization of a microchannel heat sink with temperature dependent fluid properties. Applied thermal engineering 28:1101-1107. 2008.
[13] Iverson, B. D., and S. V. Garimella. Recent advances in microscale pumping technologies: a review and evaluation. Microfluidics and nanofluidics 5:145-174. 2008.
[14] Garimella, S. V., and V. Singhal. Single-phase flow and heat transport and pumping considerations in microchannel heat sinks. Heat transfer engineering 25:15-25. 2004.
[15] Zhang, J., P. T. Lin, and Y. Jaluria. Design and optimization of multiple microchannel heat transfer systems. Journal of Thermal Science and Engineering Applications 6:011004. 2014.

[16] Ge, Y., S. Wang, Z. Liu, and W. Liu. Optimal shape design of a minichannel heat sink applying multi-objective optimization algorithm and three-dimensional numerical method. Applied Thermal Engineering 148:120-128. 2019.
[17] Zhang, X., and Y. Jaluria. Optimization of microchannel-based cooling systems. Numerical Heat Transfer, Part A: Applications 74:1053-1067. 2018.
[18] Agarwal, N., and N. R. Aluru. A domain adaptive stochastic collocation approach for analysis of MEMS under uncertainties. Journal of Computational Physics 228:7662-7688. 2009.
[19] Tu, J. A performance measure approach in reliability based structural optimization. In. University of Iowa. 1997.
[20] Tu, J., K. K. Choi, and Y. H. Park. A new study on reliability-based design optimization. Journal of mechanical design 121:557-564. 1999.
[21] George, P., J. Meng, and Y. Jaluria. Optimization of the chemical vapor deposition process for gallium nitride. In: International Heat Transfer Conference Digital Library. Begel House Inc. 2014.
[22] Sarangi, S., K. K. Bodla, S. V. Garimella, and J. Y. Murthy. Manifold microchannel heat sink design using optimization under uncertainty. International Journal of Heat and Mass Transfer 69:92-105. 2014.
[23] Shavezipur, M., K. Ponnambalam, A. Khajepour, and S. Hashemi. Fabrication uncertainties and yield optimization in MEMS tunable capacitors. Sensors and Actuators A: Physical 147:613-622. 2008.
[24] Zhang, X., and Y. Jaluria. Reliability-based optimization and design limits of microchannel cooling systems. International Journal of Heat and Mass Transfer 149:119202. 2020.
[25] Liu, Y., Y. Yang, S. Mai, D. Wang, and C. Song. Investigation into spatter behavior during selective laser melting of AISI 316L stainless steel powder. Materials & Design 87:797-806. 2015.
[26] Lee, Y., and W. Zhang. Modeling of heat transfer, fluid flow and solidification microstructure of nickel-base superalloy fabricated by laser powder bed fusion. Additive Manufacturing 12:178-188. 2016.
[27] Panwisawas, C., C. Qiu, M. J. Anderson, Y. Sovani, R. P. Turner, M. M. Attallah, J. W. Brooks, and H. C. Basoalto. Mesoscale modelling of selective laser melting: thermal fluid dynamics and microstructural evolution. Computational Materials Science 126:479-490. 2017.
[28] Shrestha, S., and K. Chou. Computational analysis of thermo-fluid dynamics with metallic powder in SLM. In: TMS Annual Meeting & Exhibition. Springer. pp 85-95. 2018.
[29] Cheng, B., X. Li, C. Tuffile, A. Ilin, H. Willeck, and U. Hartel. MULTI-PHYSICS MODELING OF SINGLE TRACK SCANNING IN SELECTIVE LASER MELTING: POWDER COMPACTION EFFECT.
[30] Khairallah, S. A., and A. Anderson. Mesoscopic simulation model of selective laser melting of stainless steel powder. Journal of Materials Processing Technology 214:2627-2636. 2014.
[31] Khairallah, S. A., A. T. Anderson, A. Rubenchik, and W. E. King. Laser powder-bed fusion additive manufacturing: Physics of complex melt flow and formation mechanisms of pores, spatter, and denudation zones. Acta Materialia 108:36-45. 2016.

[32] Matthews, M. J., G. Guss, S. A. Khairallah, A. M. Rubenchik, P. J. Depond, and W. E. King. Denudation of metal powder layers in laser powder bed fusion processes. Acta Materialia 114:33-42. 2016.
[33] Ly, S., A. M. Rubenchik, S. A. Khairallah, G. Guss, and M. J. Matthews. Metal vapor micro-jet controls material redistribution in laser powder bed fusion additive manufacturing. Scientific reports 7:4085. 2017.
[34] Yan, Z., W. Liu, Z. Tang, X. Liu, N. Zhang, M. Li, and H. Zhang. Review on thermal analysis in laser-based additive manufacturing. Optics & Laser Technology 106:427-441. 2018.
[35] Zhao, C., K. Fezzaa, R. W. Cunningham, H. Wen, F. De Carlo, L. Chen, A. D. Rollett, and T. Sun. Real-time monitoring of laser powder bed fusion process using high-speed X-ray imaging and diffraction. Scientific reports 7:3602. 2017.
[36] Gunenthiram, V., P. Peyre, M. Schneider, M. Dal, F. Coste, I. Koutiri, and R. Fabbro. Experimental analysis of spatter generation and melt-pool behavior during the powder bed laser beam melting process. Journal of Materials Processing Technology 251:376-386. 2018.
[37] Philo, A., C. Sutcliffe, S. Sillars, J. Sienz, S. Brown, and N. Lavery. A study into the effects of gas flow inlet design of the Renishaw AM250 laser powder bed fusion machine using computational modelling. Solid Free. Fabr. 2017.
[38] Philo, A., D. Butcher, S. Sillars, C. Sutcliffe, J. Sienz, S. Brown, and N. Lavery. A Multiphase CFD Model for the Prediction of Particulate Accumulation in a Laser Powder Bed Fusion Process. In: TMS Annual Meeting & Exhibition. Springer. pp 65-76. 2018.
[39] Wang, W.-C., and C.-Y. Chang. Flow analysis of the laminated manufacturing system with laser sintering of metal powder. Part I: flow uniformity inside the working chamber. The International Journal of Advanced Manufacturing Technology 92:1299-1314. 2017.
[40] Chiu, W. K., and Y. Jaluria. Continuous chemical vapor deposition processing with a moving finite thickness susceptor. Journal of Materials Research 15:317-328. 2000.
[41] Zhang, Y., L. Zhang, and C. Zhou. Review of chemical vapor deposition of graphene and related applications. Accounts of chemical research 46:2329-2339. 2013.
[42] Kawabata, T., T. Matsuda, and S. Koike. GaN blue light emitting diodes prepared by metalorganic chemical vapor deposition. Journal of applied physics 56:2367-2368. 1984.
[43] Gambit, I. Modeling Guide. Fluent Inc. 2004.
[44] Fluent, A. ANSYS Fluent Theory Guide. 2013.
[45] Gad-el-Hak, M. The MEMS handbook. CRC press. 2001.
[46] Gad-el-Hak, M. The fluid mechanics of microdevices-the Freeman scholar lecture. Transactions-American Society of Mechanical Engineers Journal of FLUIDS Engineering 121:5-33. 1999.
[47] Tuckerman, D. B. Heat-transfer microstructures for integrated circuits. In. Lawrence Livermore National Lab CA. 1984.
[48] Tuckerman, D. B., and R. Pease. High-performance heat sinking for VLSI. IEEE Electron device letters 2:126-129. 1981.
[49] Ghajar, A. J., and D. Yunus A. Cengel. Heat and Mass Transfer: Fundamentals and Applications. McGraw-Hill Education. 2014.
[50] Berne, R. M., M. N. Levy, and B. M. Koeppen. Berne & levy physiology. Elsevier Brasil. 2008.

[51] Rand, P. W., E. Lacombe, H. E. Hunt, and W. H. Austin. Viscosity of normal human blood under normothermic and hypothermic conditions. Journal of Applied Physiology 19:117-122. 1964.
[52] Zweifach, B. W. Quantitative studies of microcirculatory structure and function: I. Analysis of pressure distribution in the terminal vascular bed in cat mesentery. Circulation Research 34:841-857. 1974.
[53] Lin, P. T. Parametric Modeling and Optimization of Thermal Systems With Design Uncertainties. Rutgers The State University of New Jersey-New Brunswick. 2010.
[54] Knight, R. W., D. J. Hall, J. S. Goodling, and R. C. Jaeger. Heat sink optimization with application to microchannels. IEEE Transactions on Components, Hybrids, and Manufacturing Technology 15:832-842. 1992.
[55] Park, J., and I. W. Sandberg. Universal approximation using radial-basis-function networks. Neural computation 3:246-257. 1991.
[56] Enevoldsen, I. Reliability-based optimization as an information tool. Journal of Structural Mechanics 22:117-135. 1994.
[57] Youn, B. D., and K. K. Choi. Selecting probabilistic approaches for reliability-based design optimization. AIAA journal 42:124-131. 2004.
[58] Jumaah, O., and Y. Jaluria. The Effect of Carrier Gas and Reactor Pressure on Gallium Nitride Growth in MOCVD Manufacturing Process. Journal of Heat Transfer 141:082101. 2019.
[59] Wong, S., and Y. Jaluria. Numerical simulation of a practical chemical vapor deposition reactor. Numerical Heat Transfer, Part A: Applications 70:1057-1071. 2016.